Ablation of palladin in adult heart causes dilated cardiomyopathy associated with intercalated disc abnormalities

Giuseppina Mastrototaro,[1,2] Pierluigi Carullo,[2,3] Jianlin Zhang,[4] Beatrice Scellini,[5] Nicoletta Piroddi,[5] Simona Nemska,[2] Maria Carmela Filomena,[2,3] Simone Serio,[2] Carol A Otey,[6] Chiara Tesi,[5] Fabian Emrich,[7] Wolfgang A. Linke,[8] Corrado Poggesi,[5] Simona Boncompagni,[9] Marie-Louise Bang[2,3*]

[1]University of Milan-Bicocca, Milan, Italy. [2]IRCCS Humanitas Research Hospital, Rozzano, Milan, Italy. [3]Institute of Genetic and Biomedical Research (IRGB) - National Research Council (CNR), Milan unit, Milan, Italy. [4]University of California San Diego, School of Medicine, La Jolla, CA, USA. [5]Department of Experimental and Clinical Medicine, University of Florence, Florence, Italy. [6]Department of Cell Biology and Physiology, University of North Carolina at Chapel Hill (UNC), Chapel Hill, NC, USA. [7]Department of Cardiac Surgery, Goethe University Hospital, Frankfurt, Germany. [8]Institute of Physiology II, University of Münster, Münster, Germany. [9]Department of Neuroscience, Imaging and Clinical Sciences (DNICS) and Center for Advanced Studies and Technology (CAST), University G. d'Annunzio, Chieti, Italy.

*For correspondence: marie-louise.bang@cnr.it

Current address for Giuseppina Mastrototaro: AGC Biologics, Milan, Italy.

Abstract

Palladin (PALLD) belongs to the PALLD/myopalladin (MYPN)/myotilin family of actin-associated immunoglobulin-containing proteins in the sarcomeric Z-line. PALLD is ubiquitously expressed in several isoforms and its longest 200 kDa isoform, predominantly expressed in striated muscle, shows high structural homology to MYPN. *MYPN* gene mutations are associated with human cardiomyopathies, whereas the role of PALLD in the heart has remained unknown, partly due to embryonic lethality of PALLD knockout mice. In a yeast two-hybrid screening, CARP/Ankrd1 and FHOD1 were identified as novel interaction partners of PALLD's N-terminal region. To study the role of PALLD in the heart, we generated conditional (cPKO) and inducible (cPKOi) cardiomyocyte-specific PALLD knockout mice. While cPKO mice exhibited no pathological phenotype, ablation of PALLD in adult cPKOi mice caused progressive cardiac dilation and systolic dysfunction, associated with reduced cardiomyocyte contractility, intercalated disc abnormalities, and fibrosis, demonstrating that PALLD is essential for normal cardiac function. Double cPKO and MYPN knockout mice exhibited a similar phenotype as MKO mice, suggesting that MYPN does not compensate for the loss of PALLD in cPKO mice. Transcript levels of *MYPN* and the *PALLD* long isoform were significantly increased in myocardial tissue from human dilated cardiomyopathy patients, suggesting a role of PALLD in cardiac disease.

Introduction

Palladin (PALLD) is an actin-associated protein, which together with myopalladin (MYPN) and myotilin (MYOT) belongs to a small protein family of immunoglobulin (Ig) domain-containing proteins in the Z-line associated with the actin cytoskeleton (reviewed in (Otey, Dixon, Stack, & Goicoechea, 2009)). While MYPN and MYOT are specifically expressed in striated and skeletal muscle, respectively, PALLD is ubiquitously expressed in various tissues, including the heart, where it is expressed at high levels (Wang & Moser, 2008). Mutations in the *MYPN* gene have been associated with dilated (DCM), hypertrophic (HCM), and restrictive cardiomyopathy (Bagnall, Yeates, & Semsarian, 2010; Duboscq-Bidot et al., 2008; Meyer et al., 2013; Purevjav et al., 2012), while *MYOT* gene mutations can cause various skeletal muscle disorders (reviewed in (Otey et al., 2009)). Mutations in the *PALLD* gene have been linked to pancreatic cancer (Liotta et al., 2021; Pogue-Geile et al., 2006; Slater et al., 2007) and PALLD levels have been shown to correlate with increased invasiveness of cancer cells (Gilam et al., 2016; Goicoechea et al., 2009; von Nandelstadh et al., 2014). However, the role of PALLD in the heart has remained unknown. Whereas MYPN and MYOT are expressed as single isoforms, PALLD exists in at least 9 different isoforms due to the presence of four alternative promoters, alternative splicing, and early termination (Goicoechea et al., 2010; Wang & Moser, 2008). The longest 200 kDa isoform of PALLD, is predominantly expressed in striated muscle and highly homologous in structure to MYPN, sharing five Ig domains and a central proline-rich region (Otey et al., 2009). Furthermore, PALLD contains an additional proline-rich region, not shared with MYPN. The 140 kDa and 90-92 kDa isoforms containing four and three Ig domains, respectively, are also expressed in the heart, but have a more ubiquitous expression pattern (Wang & Moser, 2008). The expression profiles of the other isoforms have not been determined in detail (Goicoechea et al., 2010; Wang & Moser, 2008). Within the cardiac Z-line, PALLD and MYPN share several interaction partners, including α-actinin (Bang et al., 2001; Ronty, Taivainen, Moza, Otey, & Carpen, 2004), nebulette (Bang et al., 2001), titin (Filomena et

al., 2021), and members of the PDZ-LIM protein family (cypher/ZASP/LDB3, ALP/PDLIM3, CLP36/PDLIM1, RIL/PDLIM4) (von Nandelstadh et al., 2009) (illustrated in ***Figure 1A***). Furthermore, PALLD and MYPN bind to myocardin related transcription factors (MRTFs) (Filomena et al., 2020; Jin et al., 2010) as well as bind and bundle F-actin (Dixon et al., 2008; Filomena et al., 2020; Gurung et al., 2016), stabilizing the actin cytoskeleton and consequently promoting serum response factor (SRF) signaling. Additionally, PALLD binds to sorbin and SH3 domain-containing 2 (SORBS2) (Ronty et al., 2005), localized at the intercalated disc (ICD) and Z-line of the heart, as well as various proteins expressed in non-muscle cells, including actin-associated (VASP (Boukhelifa, Parast, Bear, Gertler, & Otey, 2004), ezrin (Mykkanen et al., 2001), profilin 1 (Boukhelifa et al., 2006), EPS8 (Goicoechea et al., 2006), LASP1 (Rachlin & Otey, 2006), and LPP (Jin, Kern, Otey, Wamhoff, & Somlyo, 2007)) and signaling/adaptor (SPIN90/NCKIPSD (Ronty et al., 2007), SRC (Ronty et al., 2007), and integrin β5/ITGB5 (Lai et al., 2006)) proteins.

Consistent with the interaction of PALLD with F-actin and numerous actin binding proteins, PALLD is associated with various actin-based structures, including focal adhesions, stress fibers, cell-cell junctions, and Z-lines, and is important for the assembly, organization, and maintenance of the actin cytoskeleton (reviewed in (Jin, 2011; Otey et al., 2009)). PALLD is well-known for its involvement in cell motility and smooth muscle cell differentiation, implicating it in cancer (Jin, 2011), while its role in the heart has remained elusive, in part due to embryonic lethality of PALLD knockout mice (Luo et al., 2005). Thus, to provide insights into the specific role of PALLD in cardiac muscle, we generated conditional (cPKO) and inducible (cPKOi) cardiomyocyte (CMC)-specific knockout mice for the most common PALLD isoforms. While conditional knockout of PALLD in the heart did not cause any pathological cardiac phenotype, PALLD knockdown in adult heart resulted in left ventricular (LV) dilation and systolic dysfunction, associated with fibrosis and ICD abnormalities. Furthermore, we identified cardiac ankyrin repeat protein (CARP/Ankrd1) and formin homology 2 domain containing 1 (FHOD1) as novel interaction partners to the N-terminal

region of PALLD. Quantitative real-time PCR (qRT-PCR) analyses on myocardial tissue from DCM and ischemic cardiomyopathy patients showed increased transcript levels of *MYPN* and the *PALLD* long isoform in DCM patients, suggesting a possible role of PALLD in cardiac disease

Results

The PALLD N-terminal region binds to CARP/Ankrd1 and FHOD1

To identify potential binding partners to the N-terminal region of the longest 200 kDa PALLD isoform, of which no interaction partners have previously been identified, we performed a yeast two-hybrid screening of a human heart cDNA library using the N-terminal region of human PALLD, comprising the Ig1 and Ig2 domains, as bait. Among the potential interacting proteins were cardiac ankyrin repeat protein (CARP/Ankrd1) and formin homology 2 domain containing 1 (FHOD1) (***Figure 1A*** and ***Figure 1–figure supplement 1***).

The interaction of PALLD with CARP, a transcriptional cofactor and known interaction-partner of the corresponding region of MYPN (Bang et al., 2001; Miller et al., 2003), was confirmed in a NanoBRET protein interaction assay (***Figure 1B***) and stimulated emission depletion (STED) immunofluorescence microscopy showed the localization of both CARP and PALLD in the I-band of the sarcomere (***Figure 1C***). Furthermore, PALLD was frequently found in the nucleus of CMCs, where also CARP is known to localize (***Figure 1D***) (Bang et al., 2001; Miller et al., 2003). Interestingly, two distinct polyclonal antibodies recognizing all PALLD isoforms (PALLD 622) (Pogue-Geile et al., 2006) and the PALLD C-terminal region (Proteintech Group), respectively, showed localization of PALLD in the nucleus, while a monoclonal antibody (4D10) specific for the second proline-rich region (Parast & Otey, 2000) did not stain the nucleus. Immunofluorescence stainings on CMCs from CARP knockout mice (Bang et al., 2014) showed no effect on the nuclear localization of PALLD, leaving out the possibility that CARP is responsible for the targeting of PALLD to the nucleus (***Figure 1–figure supplement 2***). We did not attempt to further narrow down

the interaction site in CARP as we previously demonstrated that full-length CARP is required for binding to MYPN (Bang et al., 2001).

FHOD1 belongs to the formin protein family involved in the regulation of the actin cytoskeleton (Al Haj et al., 2015; Dwyer, Pluess, Iskratsch, Dos Remedios, & Ehler, 2014). In the yeast two-hybrid screening, we identified two clones containing the 200 C-terminal amino acid residues of FHOD1 (***Figure 1A***). By cotransformation of PALLD with truncated FHOD1 constructs in yeast, the PALLD interaction site was further narrowed down to a region comprising the C-terminal part of the formin homology 2 (FH2) domain and part of a unique sequence before the C-terminal diaphanous autoregulatory domain (DAD) (residue 965-1052; ***Figure 1A*** and ***Figure 1–figure supplement 1B***). The FH2 domain is required for self-association of FHOD1, essential for its actin regulating activity (Madrid et al., 2005; Takeya & Sumimoto, 2003). The N-terminal region of MYPN likewise bound to FHOD1 (***Figure 1–figure supplement 1B***). The PALLD-FHOD1 interaction was confirmed in a NanoBRET protein interaction assay (***Figure 1B***) and confocal microscopy showed colocalization of PALLD with FHOD1 at the ICD as well as the Z-line where FHOD1 is present at lower levels (***Figure 1E***). At the ICD, PALLD also colocalized with its known binding partner SORBS2 (***Figure 1F***).

Conditional CMC-specific PALLD knockout mice (cPKO) exhibit normal cardiac morphology and function

To overcome the embryonic lethality of PALLD deficient mice (Luo et al., 2005), which has previously precluded the analysis of the role of PALLD in the heart, we generated *Palld* floxed ($Palld^{fl/fl}$) mice containing LoxP sites flanking exon 15 (***Figure 2–figure supplement 1A-C***). $Palld^{fl/fl}$ mice were crossed with *Myh6*-nuclear-Cre mice (Abel et al., 1999) to generate conditional CMC-specific PALLD knockout (cPKO) mice in which PALLD is ablated in developing CMCs from around embryonic day 11 (E11) (Chen et al., 2006). Efficient knockdown of the most common PALLD isoforms (200 kDa, 140 kDa, 90-92 kDa isoforms) in the heart was confirmed by qRT-

PCR (***Figure 2A***), showing a ~75% knockdown in CMCs based on levels of transcripts encoding the cardiac-specific PALLD 200 kDa isoform, which is not expressed in other cardiac cell types, such as fibroblasts and smooth muscle cells. Consistently, Western blot analysis showed nearly complete knockout of PALLD at the protein level (***Figure 2B***) with a ~95% reduction of the highest expressed 90 kDa isoform (***Figure 2C***). The expression of a smaller weakly expressed PALLD isoform of about 70 kDa was not affected. This isoform likely corresponds to a short N-terminal isoform not including exon 15, which was previously detected also in pancreas (Goicoechea et al., 2010).

The effect of PALLD knockout on cardiac morphology and function was analyzed by echocardiography. As shown in ***Figure 2–figure supplement 2A*** and ***Figure 2– figure supplement 3***, no significant differences were found between cPKO and control male mice in any of the parameters analyzed up to 6 months of age. Consistently, histological analyses showed no cardiac alterations in cPKO mice compared to control mice (***Figure 2–figure supplement 2B, C***). Furthermore, in response to mechanical pressure overload induced by transaortic constriction (TAC), no significant differences were found between cPKO and control mice as shown by echocardiography (***Figure 2D*** and ***Figure 2–source data 5***) and histological analyses (***Figure 2E*** and ***F***), although there was a tendency towards reduced contractile function in cPKO mice from 2 weeks after TAC.

Double knockout mice for PALLD and MYPN are indistinguishable from MYPN knockout mice

Due to the high structural homology between PALLD and MYPN, we hypothesized that the essentially absent cardiac pathological phenotype of cPKO mice is due to compensation by MYPN. To test this, we generated double knockout mice for PALLD and MYPN (cPKO/MKO dKO). We recently reported that MYPN knockout (MKO) mice develop LV dilation and systolic dysfunction starting from 4 months of age (Filomena et al., 2021). By echocardiography, cPKO/MKO dKO

174 (*Mypn*$^{-/-}$;*Palld*$^{fl/fl}$:Cre$^{+/0}$) mice were found to be indistinguishable from MKO mice both from the
175 MKO line and derived from the crosses as *Mypn*$^{-/-}$;*Palld*$^{fl/fl}$ littermates (***Figure 2G*** and ***Figure 2–***
176 ***source data 8***), indicating that MYPN is unlikely to compensate for the loss of PALLD in cPKO
177 mice.
178
179 **Ablation of PALLD in adult mice results in DCM and systolic dysfunction**
180 Hypothesizing that compensatory mechanisms during development prevent the development of a
181 pathological phenotype of cPKO mice, we investigated the effect of PALLD knockout in adult
182 CMCs. *Palld*$^{fl/fl}$ mice were crossed with *Myh6*-MerCreMer transgenic mice (Sohal et al., 2001) to
183 generate inducible CMC-specific PALLD knockout (cPKOi) mice, which were induced by
184 tamoxifen (TAM) injection at 7 weeks of age. Effective knockdown of the most common PALLD
185 isoforms in the heart was confirmed by qRT-PCR 8 weeks after induction, showing an about 80%
186 reduction in transcripts encoding the cardiac-specific PALLD 200 kDa isoform (***Figure 3A***).
187 Consistently, Western blot analysis on isolated CMCs showed efficient knockout of the targeted
188 isoforms (***Figure 3B***) with an ~84% knockdown of the highest expressed 90 kDa isoform (***Figure***
189 ***3C***). Like in cPKO mice, the antibody also recognized a protein of around 70 kDa present at similar
190 levels in both cPKOi mice and control mice.
191 Echocardiography showed the development of LV dilation and progressive systolic dysfunction
192 in cPKOi male mice starting from 8 weeks after induction (***Figure 3D*** and ***E***, and ***Figure 3–source***
193 ***data 3***). Intraventricular septum thickness was significantly increased 6 months after TAM
194 injection, whereas LV posterior wall thickness and heart weight to body weight were unaltered.
195 Consistent with the reduced systolic function of cPKOi mice, analysis of contractile function and
196 twitch Ca^{2+} transients in ventricular CMCs 3 months after TAM induction showed reduced
197 sarcomere shortening and Ca^{2+} transient amplitude in cPKOi mice compared to control mice
198 (***Figure 3F***). Time to peak and time to relaxation as well as the rise and decay of Ca^{2+} transients
199 were unaffected. Similarly, measurements of biomechanical properties of myofibril preparations

from the LV, showed reduced maximum Ca^{2+}-activated isometric tension (P_0) of cPKOi myofibrils compared to controls 8 weeks after TAM induction (see ***Table 1***). The kinetics of force generation and relaxation following rapid Ca^{2+} increase and removal were similar in cPKOi and control mice, indicating that the impairment of active force generation in cPKOi mice is not due to a change in the number of force generating cross-bridges. The resting tension at optimal sarcomere length between cPKOi and control preparations was not significantly different between cPKOi and control preparations (***Table 1***) and the sarcomere length-tension relationship was similar in cPKOi and control preparations, although there was a tendency towards lower resting tension at longer sarcomere lengths (***Table 1– figure supplement 1***).

Histological analyses 24 weeks after TAM induction showed interstitial fibrosis in the heart of cPKOi mice, which was not observed in control hearts (***Figure 4A*** and ***B***). No apoptosis was detected by TUNEL staining. Analysis of isolated CMCs showed increased CMC size in PKOi mice compared to control mice 3 months after TAM induction (***Figure 4C***), which was mainly due to increased CMC width (***Figure 4D*** and ***E***).

Upregulation of markers of pathological cardiac remodeling in cPKOi mouse heart

To determine the effect of PALLD knockout in adult mice on cardiac gene expression, qRT-PCR for various genes involved in cardiac remodeling, fibrosis, apoptosis, and inflammation was performed on LV RNA 6 months after TAM induction (***Figure 4–figure supplement 1***). This revealed upregulation of the cardiac stress responsive genes *Nppb*, *Myh7*, and Ankrd1 (***Figure 4F*** and ***Figure 4–figure supplement 1***), while *Nppa*, *Myh6*, *Acta1*, and *Actc1* were unaffected. In addition, although our histological analyses showed interstitial fibrosis in cPKOi hearts, no significant changes were found in the expression levels of *Col1a2*, *Col3a1*, *Ctgf*, *Tgfb1*, and *Acta2*. Consistent with the absence of apoptosis in cPKOi hearts, the antiapoptotic gene *Bcl2* was upregulated (***Figure 4F***) and the apoptosis-related genes *Bax* and *Tp53* were unaffected. No changes were found in genes encoding PALLD interacting proteins (*Nebl*, *Ldb3/Zasp/Cypher*,

Pdlim3) or other sarcomeric proteins (*Des* and *Tnnc1*). The upregulation of *Nppb*, *Myh7*, and *Ankrd1* suggests cardiac remodeling and the presence of chronic stress in the heart of cPKOi mice, consistent with an essential role of PALLD for normal heart function.

Intercalated disc abnormalities in cPKOi mouse hearts

To determine the ultrastructural effects of PALLD knockout, transmission electron microscopy (TEM) analyses were performed on papillary muscle from cPKOi and control male mice 2 and 6 months after TAM induction. The most noticeable observation was alterations in ICD ultrastructure in cPKOi mice both 2 and 6 months after TAM induction (***Figure 5***). In particular, cPKOi mice showed ICDs with abnormal ultrastructure, characterized by partial or total disruption of the ordered folded regions at the adherens junction, often showing an evidently widened amplitude (***Figure 5A***). Quantification of ICD fold amplitude (i.e. the lateral width of the folded regions indicated in ***Figure 5B***), revealed a higher, much more variable ICD fold amplitude in cPKOi compared to control mice as shown by the frequency distribution plots in ***Figure 5C*** and ***D*** (left), showing a rightward shift in cPKOi mice both at 2 and 6 months after TAM induction, with the greatest variability observed 2 months after TAM induction. Consequently, the average ICD fold amplitude was increased by ~98.7% and ~76.6% in cPKOi mice *vs*. control mice 2 and 6 months after TAM induction, respectively (***Figure 5C*** and ***D***; right). Detailed analysis of regions containing high-amplitude ICDs showed very convoluted and abnormal fold regions, often occupied by thick filaments constituting the A-band of the sarcomere with an evident disruption of the thin actin-containing filament areas normally observed within the folds of control ICDs (***Figure 5E***). Another frequent observation was the presence of structural abnormalities in the regions adjoining high-amplitude ICDs (***Figure 5F***). Specifically, while most sarcomeres had a normal organization, areas with wavy Z-lines and sarcomere disruption were present in the proximity of high-amplitude ICDs, where accumulation of vesicles was also often observed in areas of degeneration.

Based on the location of PALLD at the ICD and the ICD abnormalities observed in cPKOi

mice, we sought to examine whether PALLD ablation affects the localization or expression of other ICD proteins, including PALLD's interaction partners SORBS2 and FHOD1 as well as components of the desmosome (desmoplakin, plakoglobin/γ-catenin, plakophilin-2, desmocollin-2, desmoglein-2, desmin), adherens junction (N-cadherin, α-E-catenin, β-catenin, plakoglobin/γ-catenin, vinculin), and gap junction (connexin 43). Immunofluorescence stainings of isolated adult CMCs showed no alterations in the location of ICD proteins (***Figure 6–figure supplement 1***) and PALLD interacting proteins (***Figure 6–figure supplement 2***). However, Western blot analyses showed a ~1.5-fold increase in SORBS2 expression in the LV of cPKOi mice 2 months after TAM induction (***Figure 6A*** and ***B***). No other changes in the expression of ICD proteins were observed (Fig 6A and B). Furthermore, no changes in the levels of the PALLD homologue MYPN and PALLD-associated proteins were found (***Figure 6–figure supplement 3***). Since we recently found that PALLD binds to titin Ig-domains Z4-Z5 in the Z-line (Filomena et al., 2021) as well as indirectly to the titin N2A region via CARP (Bang et al., 2001; Miller et al., 2003), we also determined titin isoform expression and phosphorylation, both known to affect passive stiffness (Loescher, Hobbach, & Linke, 2021), but found no changes between cPKOi and control mice (***Figure 6–figure supplement 4***), consistent with absent effect of PALLD KO on resting tension (***Table 1*** and ***Table 1–figure supplement 1***). Furthermore, determination of total and phosphorylation levels of various proteins involved in cardiac signaling showed no alterations (***Figure 6–figure supplement 3***), suggesting that the DCM phenotype of cPKOi mice is caused by structural changes in the ICD.

Increased levels of transcripts encoding MYPN and the PALLD 200 kDa isoform in myocardial biopsies from human DCM patients

Our findings demonstrating an important role of PALLD for normal cardiac function, prompted us to determine whether transcript levels of *PALLD* and its striated muscle-specific homologue *MYPN* are altered during ischemic and non-ischemic cardiac disease. qRT-PCR analysis on LV biopsies from DCM and ischemic cardiomyopathy (ICM) patients *vs.* healthy control hearts (for patient

details, see ***Figure 6–figure supplement 5***) revealed a ~2.7-fold upregulation of *MYPN* mRNA in DCM patients as well as a similar ~2.5-fold upregulation of *PALLD* mRNA encoding the 200 kDa striated muscle-specific PALLD isoform, structurally homologous to MYPN (***Figure 6B***). In contrast, levels of PALLD transcripts encoding the ubiquitously expressed 140 kDa and 90-92 kDa isoforms of *PALLD* were unaltered. As previously reported, *ANKRD1*/*CARP* was upregulated in DCM patients (~4.5-fold) (Bogomolovas et al., 2015; Kempton et al., 2018; Nagueh et al., 2004; Zolk et al., 2002). None of the transcripts were altered in ICM patients.

Discussion

In the present study, we show that in addition to its known localization in the sarcomeric Z-line, PALLD is located in the I-band, the ICD, and the nucleus of CMCs. The PALLD C-terminal region was previously found to target to the nucleus in podocytes (Endlich et al., 2009) and smooth muscle cells (SMCs) (Jin et al., 2010), while the N-terminal region was shown to be required for nuclear export (Endlich et al., 2009). Consistently, immunofluorescence stainings with antibodies towards all PALLD isoforms or the PALLD C-terminal region showed the localization of PALLD in the nucleus of CMCs. However, surprisingly, antibodies against the second proline-rich region present in the major isoforms did not stain the nucleus. This suggests that only isoforms without the second proline-rich region are present in the nucleus, which is consistent with immunohistochemical stainings of human biopsies from pancreas (Goicoechea et al., 2010). PALLD isoforms containing 5, 4, and 3 Ig-domains both with and without the second proline-rich region are reported in UniProt, suggesting different cellular functions of PALLD isoforms depending on the presence of the second proline-rich region. As shown in ***Figure 1A***, many interaction partners of PALLD bind to its second proline-rich region, including SORBS2, which is present in the ICD and Z-line of the heart, so one possibility could be that the second proline-rich region tethers PALLD to the actin cytoskeleton, preventing it from going to the nucleus.

In a yeast two-hybrid screening, we identified CARP and FHOD1 as novel interaction partners of the PALLD N-terminal region for which no interaction partners have previously been identified. Since CARP is a well-known interaction partner of the MYPN N-terminal region (Bang et al., 2001), structurally homologous to the PALLD N-terminal region, it is not surprising that also PALLD binds to CARP. CARP and MYPN are known to form a complex in the I-band, where CARP is linked to the titin N2A region (Bang et al., 2001; Miller et al., 2003). Consistently, we found that also PALLD is located in the I-band, but hypothesize that only the PALLD 200 kDa isoform containing the N-terminal CARP-binding region is targeted to the I-band. Titin is a largest known protein, stretching from the Z-line to the M-line and functioning as a molecular spring responsible for the passive stiffness of striated muscle, implicating it in force transmission and mechanosensing (Loescher et al., 2021). Thus, based on their link to titin and dual localization in the sarcomere and the nucleus, CARP and MYPN were previously proposed to form a complex involved in the transduction of stretch-induced signaling from the sarcomere to the nucleus (Laure et al., 2010; Miller et al., 2003). To determine whether CARP may be responsible for the targeting of PALLD to the nucleus, we performed immunofluorescence stainings of CMCs from CARP knockout mice. However, CARP ablation did not affect the localization of PALLD in the nucleus of CMCs, questioning the hypothesis of a role of PALLD and MYPN in mechanosensing. Consistent with targeting experiments in podocytes and SMCs, it is therefore likely that the PALLD C-terminal region is responsible for its targeting to the nucleus also in CMCs. In particular, based on the binding of the PALLD Ig3 domain to the transcriptional cofactor MRTF-A (Filomena et al., 2020; Jin et al., 2010), which cycles between the cytosol and nucleus to regulate SRF signaling, it is tempting to speculate that MRTF-A is responsible for the targeting of PALLD to the nucleus. Another possibility could be that PALLD contains a nuclear localization signal (NLS), as previously predicted by sequence analysis (Endlich et al., 2009). On the other hand, no NLSs were predicted in MYPN, which is also present in the nucleus. Based on the high homology between the

two proteins, we therefore consider it most likely that PALLD and MYPN are transported to the nucleus through binding to proteins that translocate to the nucleus, such as MRTF-A.

The interaction of PALLD with FHOD1 is consistent with its location in the ICD, where it also binds to SORBS2 (Ronty et al., 2005). FHOD1 has been reported to be localized at the ICD and costamere of the heart (Al Haj et al., 2015; Dwyer et al., 2014) consistent with our findings. In contrast, Sanematsu *et al.* showed that FHOD1 is dispensable for normal cardiac development and function in mouse and failed to detect FHOD1 in the heart (Sanematsu et al., 2019). The reason for this discrepancy is unclear as several different FHOD1 antibodies were tested in each of the studies. Nevertheless, the low expression level of FHOD1 in the heart and absence of a cardiac pathological phenotype of FHOD1 deficient mice questions the relevance of the PALLD-FHOD1 interaction in CMCs. In contrast, FHOD1 is highly expressed in SMCs and other cell types, where also PALLD is present, so the interaction is likely to be important in other tissues. FHOD1 suppresses actin polymerization by inhibiting nucleation and elongation but stabilizes actin filaments by capping the actin barbed ends, protecting them from depolymerization, while simultaneously mediating F-actin bundling by connecting them to adjacent actin filaments (Schönichen et al., 2013). In line with this, FHOD1 silencing was shown to reduce migration and invasion of breast cancer cells by inhibiting the nuclear translocation of the SRF coactivator MRTF-A, which is sequestered in the cytoplasm by G-actin and regulated by changes in actin dynamics (Jurmeister et al., 2012). PALLD directly binds to MRTF-A (Filomena et al., 2020; Jin et al., 2010) and stabilizes the actin cytoskeleton by promoting actin polymerization and preventing actin depolymerization, consequently promoting MRTF-mediated activation of SRF signaling (Dixon et al., 2008; Filomena et al., 2020; Gurung et al., 2016). Thus, it is possible that PALLD and FHOD1 may cooperate in regulating actin dynamics and SRF signaling.

Global knockout of PALLD in mouse was reported to result in embryonic lethality before E15.5 due to multiple defects, including failure of body walls to close, resulting in exencephaly and herniation of abdominal organs (Luo et al., 2005). Furthermore, analysis of PALLD knockout

355 embryos revealed a key role of PALLD in the induction of SMC differentiation in the developing
356 vasculature (Jin et al., 2010) and fibroblasts derived from knockout embryos showed defects in
357 stress fiber formation, cell adhesion, and motility (Luo et al., 2005). Based on its similarity to
358 MYPN, associated with different forms of cardiomyopathy (Bagnall et al., 2010; Duboscq-Bidot et
359 al., 2008; Meyer et al., 2013; Purevjav et al., 2012), as well as high expression levels of specific
360 PALLD isoforms in cardiac muscle both during development and at adult stage, we hypothesized
361 that PALLD plays an important role also in the heart (Wang & Moser, 2008).

362 To determine the role of PALLD in the heart in vivo, we floxed *Palld* exon 15, allowing us to
363 generate conditional (cPKO) and inducible (cPKOi) CMC-specific knockout mice for all PALLD
364 isoforms except for what we believe is a small N-terminal isoform containing Ig1 and Ig2 and not
365 including exon 15. Due to extensive differential splicing of PALLD, it was not possible to target all
366 isoforms. Unexpectedly, cPKO mice exhibited no cardiac pathological phenotype at basal levels
367 and showed a normal hypertrophic response to TAC, although cPKO mice showed a tendency
368 towards reduced systolic function compared to control mice. In contrast, cPKOi mice induced at
369 adult stage developed cardiac dilation and systolic dysfunction within 8 weeks after TAM
370 induction, associated with interstitial fibrosis and upregulation of cardiac stress markers.
371 Consistently, reduced sarcomere shortening and Ca^{2+} transient amplitude were observed in CMCs,
372 and decreased maximum Ca^{2+}-activated isometric tension was found in cPKOi myofibrils, while the
373 kinetics of contraction were unaffected. The heart weight to body weight ratio was unaltered,
374 although CMC size was increased, mainly due to increased CMC width.

375 At the ultrastructural level, ICDs in cPKOi mice were disorganized and more convoluted
376 compared to those of control mice. The ICD is a highly complex structure joining together adjacent
377 CMCs in the heart and is made up of three major complexes: adherens junctions, where actin
378 filaments are anchored and connect the sarcomere to the cell membrane; desmosomes, which tether
379 the cell membrane to the intermediate filament network; and gap junctions, which permit the
380 passage of ions and small molecules between neighboring CMCs, allowing for electrical and

metabolic coupling between cells (reviewed in (Vermij, Abriel, & van Veen, 2017)). In contrast to previous belief, rather than functioning independently, the three junctions cooperate via crosstalk between their components in mixed-type junctions termed "*area composita*" (Borrmann et al., 2006; Franke, Borrmann, Grund, & Pieperhoff, 2006). Thus, the ICD can be considered as a single functional unit important for mechanical coupling and transmission of contractile force and electrical signals between adjacent CMCs. PALLD plays a well-known role in the organization of the actin cytoskeleton (Jin, 2011; Otey et al., 2009) and binds directly to F-actin (Dixon et al., 2008), ALP (von Nandelstadh et al., 2009), and SORBS2 (Ronty et al., 2005), which are associated with the adherens junction (Ding et al., 2020; Pashmforoush et al., 2001). Thus, destabilization of the adherens junction in cPKOi mice may be responsible for the structural alterations at the ICD, also affecting nearby sarcomeres, as evident by Z-line abnormalities and sarcomere disruption in the vicinity of the adherens junction in high-amplitude ICDs. PALLD also interacts with several components of the transitional junction, where the contractile apparatus is connected the ICD to allow force transmission between adjacent CMCs (Bennett, 2012). In particular, titin (Filomena et al., 2021), α-actinin (Bang et al., 2001; Ronty et al., 2004), and cypher (von Nandelstadh et al., 2009), all interaction partners of PALLD, are associated with the transitional junction, suggesting a possible effect of PALLD on the attachment of the myofilament to the ICD and the stability of the junction. Immunofluorescence stainings and Western blot analyses did not show any changes in the localization of ICD proteins, including the PALLD interaction partners FHOD1 and SORBS2. However, the protein level of SORBS2 was ~1.6-fold upregulated in cPKOi heart. SORBS2, also known as Arg kinase-binding protein 2 (ArgBP2), is a scaffold protein localized at the adherens junction of the ICD as well as the Z-line at lower levels (Ding et al., 2020). SORBS2 overexpression in mouse heart was reported to lead to upregulation of β-tubulin, a direct interaction partner of SORBS2, and consequent microtubule densification, resulting in junctophilin 2 translocation, T-tubule disorganization, defective excitation-contraction coupling, and systolic dysfunction (C. Li et al., 2020). Furthermore, SORBS was found to be upregulated in patients with

left ventricular non-compaction (LVNC), but not HCM and arrhythmogenic cardiomyopathy, and may play a role in the progression of heart failure in LVNC patients (C. Li et al., 2020). Thus, increased SORBS2 expression in cPKOi mice may contribute to ICD instability and cardiac dysfunction. ICD alterations, such as altered expression of ICD proteins and increased, more variable ICD amplitude, are commonly associated with DCM both in human and mouse (Wilson, Schoenauer, Ehler, Agarkova, & Bennett, 2014). In addition, mutations in several genes encoding ICD proteins have been associated with DCM (*VCL*, *DSP*, *DSG2, DES*) and several knockout mouse models of adheres junction and desmosomal proteins develop DCM (Bang, Bogomolovas, & Chen, 2022; Hirschy et al., 2010; Kostetskii et al., 2005; J. Li et al., 2012; Norgett et al., 2000; Sheikh et al., 2006; Zemljic-Harpf et al., 2007). Thus, it is plausible to suggest that structural alteration of the ICD in the absence of PALLD is the primary event leading to DCM and systolic dysfunction in cPKOi mice. Interestingly, MKO mice, which developed a mild form of DCM under basal conditions, also showed an increase in ICD fold amplitude, although only by ~27% and without other obvious ICD abnormalities (Filomena et al., 2021), suggesting that PALLD plays a more important structural role in the ICD than MYPN.

The absence of a pathological cardiac phenotype in cPKO mice is surprising based on the rather severe cardiac phenotype of cPKOi mice induced at adult stage. To rule out the possibility that the phenotype of cPKOi mice is due to the toxic effect of TAM, we injected cPKO with TAM and subsequently evaluated cardiac function by echocardiography. However, this did not induce any cardiac pathological phenotype, suggesting that early ablation of PALLD allows for the activation of compensatory mechanisms. Due to the structural homology of PALLD to MYPN, we hypothesized that MYPN can compensate for the absence of PALLD. However, the phenotype of cPKO/MKO dKO mice was indistinguishable from that of MKO mice, strongly suggesting that MYPN does not compensate for the loss of PALLD in cPKO mice. Another possibility is that the small N-terminal PALLD isoform not targeted by our knockout approach can compensate for the absence of the other PALLD isoforms when absent during development. However, the isoform was

not upregulated in cPKO mice and does not contain binding sites for most of the PALLD interaction partners, so we consider this rather unlikely. We hypothesize that when PALLD is knocked out during embryonic development, the mice are able to adapt through activation of compensatory mechanisms, whereas this is not anymore possible when PALLD is knocked out in adult mice. This phenomenon has also been observed in other genetic models (reviewed in (El-Brolosy & Stainier, 2017)).

Analysis of *MYPN* and *PALLD* mRNA levels in LV biopsies from human ICM and DCM patients showed a ~2.7-fold upregulation of *MYPN* and a similar ~2.5-fold upregulation of the structurally similar *PALLD* 200 kDa isoform in DCM hearts, while the expression of the 140 and 90 PALLD isoforms were unaltered. For comparison, in two RNA-Seq studies, MYPN was reported to be ~1.6 upregulated in DCM/non-ischemic cardiomyopathy (NICM) and ~1.5 to ~1.7 fold upregulated in ICM hearts *vs*. healthy control hearts (Sweet et al., 2018; Yang et al., 2014), confirming the upregulation of *MYPN* transcripts in DCM patients. The higher upregulation of *MYPN* in DCM patients and absent modulation in ICM patients found in the present study may be because of different patient cohorts and detection methods used. In contract to the present study, where we found a ~2.5-fold upregulation of the 200 kDa PALLD isoform, the two RNA-Seq studies reported a ~1.6 to ~2.1-fold downregulation of PALLD in both DCM/NICM and ICM patients. The apparent discrepancy can be explained by the fact that only the PALLD 200 kDa isoform is upregulated in DCM patients, while the RNA-Seq studies do not distinguish between different PALLD isoforms. The specific upregulation of only the PALLD 200 kDa isoform suggests that it has a specific function in the heart, consistent with its predominant expression in striated muscle. Future studies will be required to determine the significance of the upregulation of MYPN and the PALLD 200 kDa isoform in DCM and whether the two genes may represent potential biomarkers.

Altogether, our data demonstrate an important role of PALLD for normal heart function, suggesting PALLD as a possible candidate gene for cardiomyopathy. Based on the absence of a

phenotype in PKO mice, loss-of-function mutations are unlikely to affect cardiac function and would likely lead to embryonic lethality due to the essential role of PALLD in other tissues and cell types. However, as for MYPN, whose ablation does not severely affect cardiac function, it is possible that mutations with dominant negative effects, especially within the 200 kDa PALLD isoform principally expressed in striated muscle, may be linked to cardiac disease. The reason why as of yet a link between *PALLD* mutations to cardiac disease has not been established could be due to lack of focus on the *PALLD* gene.

Materials and Methods

Key Resources Table

Reagent type (species) or resource	Designation	Source or reference	Identifiers	Additional information
Strain, strain background (male *M. musculus*)	MYPN knockout (MKO) mice (C57BL/6J background)	Filomena et al., 2020	N/A	
Strain, strain background (male *M. musculus*)	PALLD floxed mice (C57BL/6J background)	This paper	N/A	
Strain, strain background (male *M. musculus*)	*Myh6*-nuclear-Cre mice (C57BL/6J background)	Abel et al., 1999	N/A	
Strain, strain background (male *M. musculus*)	*Myh6*-MerCreMer transgenic mice (C57BL/6J background)	Sohal et al., 2001	N/A	
Strain, strain background (*M. musculus*)	C57BL/6J	The Jackson Laboratories	Cat# 000664 RRID:IMSR_JAX:000664	
Strain, strain background (*E. coli*)	DH5α electrocompetent cells	New England BioLabs	Cat# C2989K	
Strain, strain background (*S. cerevisiae*)	Y2H Gold yeast strain	Takara Bio	Cat# 630498	

Strain, strain background (*Saccharomyces cerevisiae*)	L40 yeast strain	Takara Bio	N/A	
Antibody	anti-PALLD 622 (rabbit polyclonal)	Pogue-Geile et al., 2006	Kindly provided by Prof. Carol Otey, University of North Carolina, Chapel Hill, NC, USA	WB (1:500) IF (1:30)
Antibody	Anti-PALLD Proteintech (rabbit polyclonal)	Proteintech Group	Cat# 10853-1-AP	WB (1:1000) IF (1:30)
Antibody	Anti-PALLD 1E6 (mouse monoclonal)	Parast and Otey, 2000 Novus Biochemicals	Cat# NBP1-25959	WB (1:1000) IF (1:20)
Antibody	Anti-PALLD 4D10 (mouse monoclonal)	Parast and Otey, 2000	N/A	IF (1:10)
Antibody	anti-MYPN (rabbit polyclonal)	Yamamoto et al., 2013	N/A	WB (1:1000)
Antibody	anti-nebulette (rabbit polyclonal)	Mastrototaro et al., 2015	N/A	WB (1:200) IF (1:20)
Antibody	anti-α-actinin (mouse monoclonal)	Merck Life Science	Cat# A7811 RRID:AB_476766	WB (1:50000) IF (1:250)
Antibody	anti-ANKRD1/CARP (rabbit polyclonal)	Miller et al., 2003	N/A	WB (1:200) IF (1:20)
Antibody	anti-Cypher (rabbit polyclonal)	Zhou *et al*., 2013	Kindly provided by Prof. Ju Chen, University of California San Diego, La Jolla, CA, USA	WB (1:500) IF (1:20)
Antibody	anti-MKL1/MRTF-A (rabbit polyclonal)	Santa Cruz Biotechnology	Cat# sc-21558	WB (1:500) IF (1:20)
Antibody	anti-MKL1/MRTF-A (rabbit polyclonal)	Immunological Sciences	Cat# AB-84312 RRID:AB_2892156	WB (1:500)

Antibody	Calpain 3	(König et al., 2003)	Kindly provided by Prof. Ahmed Ouali, QuaPA, INRA de Clermont Ferrand - Theix, St Genès Champanelle, France.	WB (1:500)
Antibody	anti-desmin (rabbit polyclonal)	Abcam	Cat# Ab8592 RRID:AB_306653	IF (1:80)
Antibody	Anti-SORBS2 (mouse monoclonal)	Merck Life Science	Cat# SAB4200183 RRID:AB_10638778	WB (1:750) IF (1:30)
Antibody	Anti-FHOD1 (goat polyclonal)	Santa Cruz Biotechnology	Cat# sc-46965 RRID: AB_2247011	WB (1:500) IF (1:30)
Antibody	Anti-desmoplakin 1/2 (mouse monoclonal)	Bio-Rad Laboratories	Cat# 2722-5204 RRID:AB_619950	WB (1:750) IF (1:20)
Antibody	Anti-N-cadherin (mouse monoclonal)	Cell Signaling Technology	Cat# 4061 RRID:AB_10694647	WB (1:1000) IF (1:80)
Antibody	anti-α-E-catenin (mouse monoclonal)	Santa Cruz Biotechnology	Cat# sc-9988 RRID:AB_626805	WB (1:1000) IF (1:20)
Antibody	anti-β-catenin (rabbit monoclonal)	Cell Signaling Technology	Cat# 8480 RRID:AB_11127855	WB (1:1000) IF (1:25)
Antibody	anti-γ-catenin/ plakoglobin (rabbit polyclonal)	Immunological Sciences	AB-90215 RRID:AB_2892157	WB (1:1000) IF (1:20)
Antibody	Anti-vinculin (mouse monoclonal)	Merck Life Science	Cat# V9264 RRID:AB_10603627	WB (1:2000) IF (1:80)
Antibody	Anti-desmocollin 2 (rabbit monoclonal)	Fitzgerald	Cat# 20R-RRID: DR004AB_1284102	IF (1:50)

Antibody	Anti-desmoglein 1 + 2 (mouse monoclonal)	Fitzgerald	Cat# 10R-D105A RRID: AB_1284107	WB (1:500) IF (1:30)
Antibody	Anti-plakophilin 2 (mouse monoclonal)	Fitzgerald	Cat# 10R-P130B RRID: AB_1288393	IF (1:50)
Antibody	Anti-connexin 43 (mouse monoclonal	Thermo Fisher Scientific	Cat# 35-5000 RRID:AB_87322	WB (1:400) IF (1:50)
Antibody	Anti-Smad1/5-Ser463/465/Smad8-Ser426/428 (rabbit polyclonal)	Cell Signaling Technology	Cat# 9511 RRID: AB_331671	WB (1:1000)
Antibody	Anti-PKCα (rabbit polyclonal)	Cell Signaling Technology	Cat# 2056 RRID: AB_2284227	WB (1:1000)
Antibody	Anti-pPDK-Ser241 (rabbit polyclonal)	Cell Signaling Technology	Cat# 3438 RRID: AB_2161134	WB (1:1000)
Antibody	anti-Akt (rabbit polyclonal)	Cell Signaling Technology	Cat# 9272 RRID:AB_329827	WB (1:1000)
Antibody	Anti-pAkt-Thr308 (rabbit polyclonal)	Cell Signaling Technology	Cat# 2965 RRID: AB_2255933	WB (1:500)
Antibody	Anti-pAkt-Ser473 (rabbit polyclonal)	Cell Signaling Technology	Cat# 4060 RRID: AB_2315049	WB (1:500)
Antibody	Anti-pGSK3β-Ser9 (rabbit polyclonal)	Cell Signaling Technology	Cat# 5558 RRID: AB_10013750	WB (1:500)
Antibody	Anti-GSK3β (rabbit polyclonal)	Cell Signaling Technology	Cat# 9315 RRID: AB_490890	WB (1:1000)
Antibody	Anti-pP70-Ser6K-Thr421/Ser424 (rabbit polyclonal)	Cell Signaling Technology	Cat# 9204 RRID: AB_2265913	WB (1:500)
Antibody	Anti-P70-Ser6K (rabbit polyclonal)	Cell Signaling Technology	Cat# 2708 RRID: AB_390722	WB (1:500)
Antibody	Anti-pMEK1/2-Ser217/221	Cell Signaling Technology	Cat# 9154 RRID:	WB (1:500)

	(rabbit polyclonal)		AB_2138017	
Antibody	anti-pErk1/2-Thr202/Tyr204 (rabbit polyclonal	Cell Signaling Technology	Cat# 4370 RRID:AB_2315112	WB (1:500)
Antibody	anti-Erk1/2 (mouse monoclonal)	Santa Cruz Biotechnology	Cat# sc-514302 RRID:AB_2571739	WB (1:1000)
Antibody	Anti-pP38-Thr180/Tyr182 (rabbit polyclonal)	Cell Signaling Technology	Cat# 4631 RRID: AB_331765	WB (1:500)
Antibody	anti-P38α/β (mouse monoclonal)	Santa Cruz Biotechnology	Cat# sc-7972 RRID:AB_628079	WB (1:500)
Antibody	Anti-phosphoserine/threonine (rabbit polyclonal)	ECM Biosciences	Cat#PP2551 RRID: AB_1184778	WB (1:500)
Antibody	Anti-phosphoserine/ threonine (rabbit polyclonal)	ECM Biosciences	Cat# PP2551 RRID:AB_1184778	WB (1:500)
Antibody	Anti-pTTN-Ser3991 (rabbit polyclonal)	Kotter et al., 2013	N/A	WB (1:500)
Antibody	Anti-pTTN-Ser4080 (rabbit polyclonal)	Kotter et al., 2013	N/A	WB (1:500)
Antibody	Anti-pTTN-Ser12742 (rabbit polyclonal)	Kotter et al., 2013	N/A	WB (1:500)
Antibody	Anti-GAPDH (rabbit polyclonal)	Proteintech	Cat# 10494-1-AP RRID: AB_2263076	WB (1:15000)
Antibody	Goat anti-mouse IgG (H + L) Highly-cross Adsorbed Secondary antibody, Alexa Fluor 488-conjugated IgG	Thermo Fisher Scientific	Cat# A11029 RRID:AB_138404	IF (1:500)
Antibody	Goat anti-rabbit IgG (H + L) Highly-cross Adsorbed	Thermo Fisher Scientific	Cat# A11034 RRID:AB_2576217	IF (1:500)

	Secondary antibody, Alexa Fluor 488			
Antibody	Goat anti-mouse IgG (H + L) Highly-cross Adsorbed Secondary antibody, Alexa Fluor 568	Thermo Fisher Scientific	Cat# A11031 RRID:AB_144696	IF (1:500)
Antibody	Goat anti-rabbit IgG (H + L) Highly-cross Adsorbed Secondary antibody, Alexa Fluor 568	Thermo Fisher Scientific	Cat# A11036 RRID:AB_10563566	IF (1:500)
Antibody	Goat anti-mouse IgG (H + L) Highly-cross Adsorbed Secondary antibody, Alexa Fluor 647	Thermo Fisher Scientific	Cat# A21236 RRID:AB_2535805	IF (1:500)
Antibody	Goat anti-rabbit IgG (H + L) Highly-cross Adsorbed Secondary antibody, Alexa Fluor 647	Thermo Fisher Scientific	Cat# A21245 RRID:AB_2535813	IF (1:500)
Antibody	Goat anti-rabbit IgG Horseradish Peroxidase (HRP)	Thermo Fisher Scientific	Cat# 31460 RRID:AB_228341	WB (1:5000)
Antibody	Goat anti-mouse IgG-HRP	Thermo Fisher Scientific	Cat# 31430 RRID:AB_228307	WB (1:5000)
Antibody	Donkey anti-goat IgG-HRP	Santa Cruz Biotechnology	Cat# sc-2020 RRID:AB_631728	WB (1:2000)
Recombinant DNA reagent	pGBKT7 DNA-BD vector	Takara Bio	Cat# 630443	
Recombinant DNA reagent	pGADT7 AD vector	Takara Bio	Cat# 630442	
Recombinant DNA reagent	Mate & Plate™ Human Heart library	Takara Bio	Cat# 630471	

Recombinant DNA reagent	pGBKT7 human MYPN N-term start-Ig2 (bp 233-1798; aa. 1-522; NM_032578.3)	This paper	N/A	Cloning primers in Supplementary file 1
Recombinant DNA reagent	pGBKT7 human MYPN C-term Ig3-end (bp 3044-4195; aa. 938-1320; NM_032578.3)	This paper	N/A	Cloning primers in Supplementary file 1
Recombinant DNA reagent	pGBKT7 human MYPN full-length	This paper	N/A	Cloning primers in Supplementary file 1
Recombinant DNA reagent	pGBKT7 human PALLD full-length	This paper	N/A	Cloning primers in Supplementary file 1
Recombinant DNA reagent	pGBKT7 human PALLD N-term start-Ig2 (bp 212-1795; aa. 1-528; NM_001166108)	This paper	N/A	Cloning primers in Supplementary file 1
Recombinant DNA reagent	pGBKT7 mouse PALLD C-term Ig3-end (bp 1146-2309; aa 267-680; BC127081)	This paper	N/A	Cloning primers in Supplementary file 1
Recombinant DNA reagent	pGADT7-AD human CARP full-length	This paper	N/A	Cloning primers in Supplementary file 1
Recombinant DNA reagent	pGADT7-AD human FHOD1 (bp 3005-3607, aa. 965-1164; NM_013241.2)	This paper	N/A	Cloning primers in Supplementary file 1
Recombinant DNA reagent	pGADT7-AD human FHOD1 (bp3005-3268, aa. 965-1052; NM_013241.2)	This paper	N/A	Cloning primers in Supplementary file 1
Recombinant DNA reagent	pGADT7-AD human FHOD1 (bp 3152-3607, aa. 1014-1164; NM_013241.2)	This paper	N/A	Cloning primers in Supplementary file 1
Recombinant DNA reagent	pFN21A HaloTag CMV Flexi vector human PALLD full-length	This paper	N/A	Cloning primers in Supplementary file 1
Recombinant	pNLF1-N [CMV	This paper	N/A	Cloning primers in

DNA reagent	Hygro] mouse FHOD1 Y2H clone (bp3106-3711, aa. 997-1197; NM_013468.3			Supplementary file 1
Recombinant DNA reagent	pNLF1-C [CMV Hygro] mouse CARP (bp 64-1023; aa. 1-319; NM_013468.3)	This paper	N/A	Cloning primers in Supplementary file 1
Sequence-based reagent	qRT-PCR primers	This paper	N/A	Supplementary file 1
Commercial assay or kit	In-Fusion HD Cloning kit	Takara Bio	Cat# 639650	
Commercial assay or kit	DC™ Protein Assay Kit II	Bio-Rad Laboratories	Cat# 5000112	
Commercial assay or kit	Frozen-EZ Yeast Transformation II kit	Zymo Research	Cat# T2001	
Commercial assay or kit	HaloTag NanoBRET 618 Ligand	Promega	Cat# G9801	
Chemical compound, drug	Aureobasidin A	Takara Bio	Cat# 630499	
Chemical compound, drug	X-α-Gal	Takara Bio	Cat# 630463	
Chemical compound, drug	PureZOL RNA isolation reagent	Bio-Rad Laboratories	Cat# 7326890	
Chemical compound, drug	High Capacity cDNA Reverse Transcription kit	Thermo Fisher Scientific	Cat# 4368814	
Chemical compound, drug	SYBR Select Master Mix	Thermo Fisher Scientific	Cat# 4472903	
Chemical compound, drug	Roche cOmplete Protease Inhibitor Cocktail	Thermo Fisher Scientific	Cat# 11697498001	
Chemical compound, drug	Pierce™ Phosphatase Inhibitor Mini Tablets	Thermo Fisher Scientific	Cat# A32957	
Chemical compound, drug	Immobilon™ Western Chemiluminescent HRP Substrate	Merck Life Science	Cat# WBKLS0500	
Chemical	Rhodamine	Thermo Fisher	Cat# R415	IF (1:100)

compound, drug	phalloidin	Scientific		
Chemical compound, drug	Wheat Germ Agglutinin, Alexa Fluor™ 594 Conjugate	Thermo Fisher Scientific	Cat# W11262	IF (1:500)
Chemical compound, drug	VECTASHIELD® Vibrance™ Antifade Mounting Medium with DAPI	D.B.A Italia Srl.	Cat# H-1800-10	
Chemical compound, drug	Liberase Blendzyme	Roche Diagnostics	Cat# 11988468001	
Chemical compound, drug	Fura-2, AM, cell permeant	Thermo Fisher Scientific	Cat# F1201	
Software, algorithm	Prism, version 7.0	GraphPad Software Inc.	https://www.graphpad.com/scientific-software/prism/ RRID:SCR_002798	
Software, algorithm	Fiji (ImageJ) analysis software, version 2.0.0-rc-69/1.52p)	National Institute of Health (NIH)	https://fiji.sc/ RRID:SCR_002285	SparkMaster plugin used for Ca^{2+} spark analysis
Software, algorithm	NT Affinity Analysis software, version 2.0.1334	NanoTemper Technologies	N/A	
Software, algorithm	Ion Wizard, software, version 6.6.11	IonOptix B.V.	N/A	

Animal experiments

All animal experiments were approved by the Italian Ministry of Health (Approval 12/2011) and performed in full compliance with the rules and regulations of the European Union (Directive 2010/63/EU of the European Parliament) and Italy (Council of 22 September 2010; directive from the Italian Ministry of Health) on the protection of animal use for scientific purposes. Mice used for experiments were sacrificed by cervical dislocation under isoflurane anesthesia. Animals were randomly assigned to different experimental groups before the start of experiments. The investigators were blinded to genotype and treatment.

Generation of conditional (cPKO) and inducible (cPKOi) cardiac muscle specific PALLD KO mice

Palld genomic DNA was obtained from a 129SVJ mouse genomic library (Stratagene, La Jolla, CA) and used for the generation of a targeting construct containing *loxP* sites flanking exon 15 (according to the nomenclature of Wang and Moser (Wang & Moser, 2008); GGGGTTCCCAAAGAAGTCCAGTAGAACTGCTAGAATTGCCTCTGATGAGGAGATTCAA GGCACAAAGGATGCTGTCATCCAAGACCTGGAACGGAAGCTTCGCTTCAAGGAGGACC TTCTGAACAATGGCCAACCG; NCBI Gene ID: 72333) as well as a neomycin (neo) cassette flanked by Flpase Recognition Target (FRT) sites. Exon 15 was floxed, since it is present in the most common PALLD isoforms (90-92 kDa, 140 kDa, 200 kDa) and contains a number of nucleotides not evenly dividable by 3, so that Cre-mediated recombination would result in an early stop codon and consequent mRNA degradation. The construct was generated in the pBluescript II KS+ vector, and the 5′ arm of homology consisted of a 3,983 bp *Not*I–*Eco*RV fragment (5' forward: gctccaccgcggtggcggccgc/AGAGCAGTTATCCTAAG; 5' reverse: gttatattaagggttccggatcgatgatatc/AACATGAAATG) fused with a *loxP* site upstream of *Palld* exon 15. The 3′ arm of homology was a 3,062 kb *Sal*I–*Sal*I fragment (3' forward: ccaagctgatcctctagagtcgac/TCCATGAGGCTCTGTC, and 3' reverse: cgggcccccctcgaggtcgac/GGAAAGGAAAACACAG) located downstream of exon 15 followed by a FRT-neo-FRT cassette and a second *loxP* site (***Figure 2–figure supplement 1***). The Diphteria toxin A fragment (DTA) gene was inserted for negative selection. The final targeting construct was verified by sequencing and linearized with *Not*I before electroporation into R1 embryonic stem (ES) cells at the Transgenic Core Facility at the University of California San Diego. G418-resistant ES clones were screened for homologous recombination by Southern blot analysis of *Eco*RV-digested ES cell DNA with a 471 bp probe generated by PCR on mouse genomic DNA with *palld* specific primers (sense: ATTCTTGAATGTATGGTGCCCTTGA; reverse:

CTCAAAGCAGACCTCATCACAAAAC) (see ***Figure 2–figure supplement 1A*** and ***B***). The wild-type allele is represented by the band of 19,607 bp, whereas the 10,130 bp band represents the correctly targeted mutant allele. One clone out of 480 G418-resistant ES clones that had undergone homologous recombination was identified. The homologous recombinant ES clone was microinjected into C57BL/6J blastocysts and transferred into pseudopregnant mice. Male chimeras were bred with female C57BL/6J mice to generate germ line transmitted heterozygous *Palld* floxed (*Palld*$^{fl/+}$) mice, which were crossed with FLPe deleter mice (KANKI, SUZUKI, & ITOHARA, 2006) to remove the *neo* gene and subsequently backcrossed for 6 generations with C57BL/6J mice. To generate conditional cardiac specific knockout (cPKO) mice, homozygous *Palld* floxed (*Palld*$^{fl/fl}$) mice were interbreed with *Myh6*-nuclear-Cre (Abel et al., 1999) mice. The resulting *Palld*$^{fl/+}$;Cre$^{+/0}$ mice were crossed with *Palld*$^{fl/+}$;Cre$^{0/0}$ mice to generate *Palld*$^{fl/fl}$;Cre$^{+/0}$ mice as cPKO mice and *Palld*$^{fl/fl}$;Cre$^{0/0}$ (*Palld*$^{fl/fl}$) mice as littermate controls. Furthermore, *Palld*$^{+/+}$;Cre$^{+/0}$ (Cre$^{+/0}$) mice derived from the same crossings were used as additional controls. Genotyping was performed on mouse tail DNA using PALLD specific primers (sense: GCTTCGCTTCAAGGAGGACCTTCTG; reverse: TGTATATCATGTTGTGGTGTCAGCC), giving rise to a 348 band for the wild-type allele and a 418 band for the targeted allele (***Figure 2–figure supplement 1C***). The presence of Cre was verified using Cre specific primers (sense: ACGTTCACCGGCATCAACGT, reverse: CTGCATTACCGGTCGATGCA), giving rise to a 356 bp band (***Figure 2–figure supplement 1C***). Inducible cardiac specific knockout (cPKOi) mice were generated by interbreeding of *Palld*$^{fl/fl}$ mice with *Myh6*-MerCreMer (MCM) transgenic mice (Sohal et al., 2001). Knockout of *Palld* in cPKOi (*Palld*$^{fl/fl}$;MCM$^{+/0}$) male mice was induced at 7 weeks of age by intraperitoneal injection of TAM dissolved in sesame oil (30 mg/kg/day) for 5 days, a dose that does not produce toxicity in mice. TAM-treated *Palld*$^{fl/fl}$;MCM$^{0/0}$ (*Palld*$^{fl/fl}$) and *Palld*$^{+/+}$;MCM$^{+/0}$ (MCM$^{+/0}$) mice as well as *Palld*$^{fl/fl}$;MCM$^{+/0}$ mice not receiving TAM served as controls. Double knockout mice (cPKO/MKO dKO) for PALLD and MYPN were generated by interbreeding of *Palld*$^{fl/fl}$;Cre$^{+/0}$ mice with *Mypn*$^{-/-}$ mice, giving rise to *Mypn*$^{-/-}$;*Palld*$^{fl/fl}$;Cre$^{+/0}$ mice

as cPKO/MKO dKO mice and *Mypn*$^{-/-}$;*Palld*$^{fl/fl}$ mice control mice derived from the same crosses. All experiments were performed on male mice as females often develop a less severe cardiac phenotype due to the cardioprotective role of estrogen (Brower, Gardner, & Janicki, 2003; Du, 2004).

In vivo cardiac physiology

Mice anaesthetized by inhalation of 1% isoflurane were subjected to transthoracic echocardiography using a Vevo 2100 System (VisualSonics) and a 30 MHz probe as previously described (Tanaka et al., 1996). Transverse Aortic Constriction (TAC) was executed with a 27-gauge needle on 8-week-old cPKO and control mice anaesthetized by intraperitoneal injection of a mixture of ketamine (100 mg/kg) and xylazine (5 mg/kg) as described (Tanaka et al., 1996). Cardiac morphology and function were assessed by transthoracic echocardiography and the pressure gradient was evaluated by Doppler echocardiography. Only mice with a pressure gradient >70 mmHg were included in the analysis. Sham-operated mice were used as controls.

Human tissue

Human myocardial tissue was collected from the apex of patients with ICM or DCM during left ventricular assist device (LVAD) implantation at Leipzig Heart Center in Germany following approval by the institutional review board (protocol #240/16-ek) and signed informed consent from the patients according to the principles of the Declaration of Helsinki. Myocardial tissue from five healthy donors rejected for transplantation was obtained from Careggi University Hospital, Florence, Italy (protocol #2006/0024713; renewed May 2009). All patients were Caucasian. Myocardial tissue was immediately snap frozen in liquid nitrogen and stored at -80°C for further processing.

DNA constructs

555 Human *PALLD*, *MYPN*, *FHOD1*, and *ANKRD1* cDNAs, isolated by PCR using available constructs
556 or a human cDNA library as a template, were cloned into pGBKT7 DNA-BD (Takara Bio),
557 pGADT7-AD (Takara Bio), pFN21A HaloTag CMV Flexi (Promega), pNLF1-N [CMV Hygro]
558 (Promega), and pNLF1-C [CMV Hygro] (Promega) vectors using restriction cloning or the In-
559 Fusion HD Cloning Plus kit (Takara Bio) according to the manufacturer's instructions. Primer
560 sequences are listed in ***Supplementary file 1***. All constructs were confirmed by sequencing.
561

562 **Yeast two-hybrid assays**

563 Yeast two-hybrid screening was performed using the Matchmaker Gold Yeast Two-Hybrid System
564 (Takara Bio) as described by the manufacturer (Young, Ferguson, Banuelos, & Gautel, 1998).
565 Briefly, cDNA encoding the N-terminal region of human PALLD comprising Ig1 and Ig2 (amino
566 acids 1-528) was cloned into the pGBKT7 DNA-BD bait vector (see *Supplementary Table S6*) and
567 transformed into the yeast two-hybrid Gold yeast strain. The bait stain was combined with a Mate &
568 Plate^{TM} Human Heart library (Takara Bio) for 24 hours after which cells were plated on selective
569 synthetic defined (SD) agar plates lacking tryptophan, leucine, histidine, and adenine and
570 containing 120 ng/mL Aureobasidin A (SD/–Ade/–His/–Leu/–Trp/AbA). Colonies appearing after
571 3-4 days of incubation at 30°C were restreaked onto SD/–Ade/–His/–Leu/–Trp/AbA/X-α-Gal plates
572 containing 40 µg/mL X-α-Gal, after which library plasmids from blue clones were isolated and
573 sequenced. To confirm the interactions and narrow down the binding sites, pGBKT DNA-BD and
574 pGADT7-AD vectors (Takara Bio) containing cDNAs encoding regions of MYPN, PALLD,
575 CARP, and FHOD1 were cotransformed into the yeast two-hybrid Gold yeast strain and spotted on
576 SD/–Ade/–His/–Leu/–Trp/AbA/X-α-Gal plates. Interaction was verified after 3-4 days of
577 incubation at 30°C. Successful transformation of the two plasmids was confirmed by growth on
578 SD/-Trp/-Leu plates. Possible autoactivation of bait and prey constructs was tested by
579 cotransformation of the bait or prey vector with empty prey or bait vector, respectively.
580

NanoBRET protein:protein interaction assay

HEK293 cells cotransfected with pFN21A HaloTag CMV Flexi vector (Promega) expressing PALLD and pNLF1-N [CMV Hygro] or pNLF1-C [CMV Hygro] vector (Promaga) expressing ANKRD1 were treated with 100 nM HaloTag NanoBRET 618 Ligand (Promega), whereafter signals were detected six hours later using a Synergy 4 instrument (BioTek). Results were analyzed using GraphPad Prism 9.0 software.

RNA extraction and quantitative qRT-PCR

LV RNA from mice or patients was extracted using PureZOL RNA isolation reagent (Bio-Rad Laboratories) according to the manufacturer's instructions. For qRT-PCR, first-strand cDNA synthesis was performed using the High Capacity cDNA Reverse Transcription kit (Thermo Fisher Scientific), whereafter qRT-PCR was performed in triplicate with custom designed oligos (see ***Supplementary file 1***) using the SYBR Select Master Mix (Thermo Fisher Scientific). Relative expression analysis was performed using the ΔΔCt method using *Gapdh* (mice) or *HPRT* (human) for normalization.

Isolation of adult ventricular CMCs

For isolation of ventricular CMCs, hearts were cannulated and mounted on a Langendorff perfusion apparatus and perfused with Hank's Balanced Salt Solution (HBSS w/o $CaCl_2$ and $MgCl_2$) supplemented with 1.2 mM MgSO4, 15 mM glucose, 30 mM Taurine, and 1 mM $MgCl_2$ hexahydrate for 10 min at 37°C. Liberase blendzyme (Roche) (50 µg/ml) was then added to the solution and perfusion was continued for about 10 min until the heart became flaccid. Subsequently, the heart was removed and cells were dissociated and filtered through a 70 µm filter after which BSA (Merck Life Science) was added to a final concentration of 4% to inactivate the enzyme. The cells were then allowed to settle and resuspended in fresh solution. For determination of CMC size, length, and width, pictures were taken on an Olympus BX53 Fluorescent microscope and analyzed

using ImageJ, version 2.1.0/1.53 C (NIH).

CMC contractility and intracellular Ca^{2+} transient measurements

Simultaneous measurements of CMC contractility and Ca^{2+} transients were carried out on an IonOptix system as previously described (Kondo et al., 2006). Briefly, CMCs loaded with 1 µM of the Ca^{2+} probe Fura-2 AM (Thermo Fisher Scientific) were placed in a perfusion system and continuously perfused with perfusion buffer (HBSS without Ca^{2+} and Mg^{2+}, supplemented with 1.2 mM $MgSO_4$, 15 mM glucose, 30 mM taurine, and 1.0 mM $MgCl_2$), containing 1.0 mM $CaCl_2$ at 37°C at a constant flow rate of 1 ml/min. Loaded cells were paced (25 V) via two electrodes at frequencies of 0.5, 1.0 and 2.0 Hz, and sarcomere shortening and Fura-2 ratio (measured at 512 nm upon excitation at 340 and 380 nm) were simultaneously recorded on a Nikon Eclipse TE-2000S inverted fluorescence microscope with a 40x/1.3 N.A. objective and an attached CCD camera (MyoCam-S, IonOptix). Data acquisition and analysis were performed using Ion Wizard software, version 6.6.11 (IonOptix).

Mechanical experiments in isolated myofibrils

Mechanical data were collected at 15°C from small bundles of cardiac myofibrils from frozen ventricular strips of cPKOi and control mice as previously described (Kreutziger et al., 2011). Briefly, thin myofibril bundles (1-4 µm width, initial sarcomere length around 2.2 µm) were maximally Ca^{2+}-activated (pCa 4.5) and fully relaxed (pCa 8.0) by fast solution switching. Maximal tension and the kinetics of force activation, and force relaxation were measured.

Histology and immunofluorescence stainings

For histology, mouse hearts were harvested, relaxed in 50 mM KCl in PBS, and fixed overnight in 4% paraformaldehyde (PFA) in PBS. Subsequently, hearts were dehydrated, embedded in paraffin, and cut in 8 µm sections in the four-chamber view. Briefly, heart sections were stained with

633 hematoxylin and eosin or Picro Sirius Red and imaged using a VS20 DotSlide Digital Virtual
634 Microscopy System (Olympus). The area of fibrosis in the LV was determined using *ad*
635 *hoc* software automatically detecting Picro Sirius Red-stained areas based on RGB color
636 segmentation (Grizzi et al., 2019). The sum of Picro Sirius Red-stained areas was expressed as a
637 percentage of the LV area excluding unfilled and tissue-free spaces. For immunostaining of
638 cryosectioned heart, the upper half of the heart was relaxed in 50 mM KCl in PBS, fixed for 15 min
639 in 4% PBS, and subsequently saturated in 15% and 30% sucrose in PBS and frozen in OCT. 10 μm
640 sections were permeabilized and blocked for 1 hour in blocking solution containing 5% normal goat
641 serum, 0.3% Triton X-100, and 50 mM glycine in PBS after which sections were incubated with
642 primary antibodies in wash buffer (blocking buffer diluted 10 times in PBS) overnight at 4°C. After
643 washing in wash buffer, sections were incubated at room temperature for 4 hours with rhodamine-
644 labeled phalloidin (1:100, Merck Life Science) and/or Alexa-Fluor-488 or -568-conjugated IgG
645 secondary antibodies (1:500, Thermo Fisher Scientific). The primary and secondary antibodies used
646 are listed in the ***Key Resources Table***. For immunostaining of adult CMCs, CMCs were fixed for 5
647 min in 4% PFA in PBS and subsequently plated on laminin-coated 8-well Nunc™ Lab-Tek™
648 Chamber Slides (Thermo Fisher Scientific). CMCs were permeabilized and blocked for 1 hour in
649 blocking solution containing 5% normal goat serum and 0.2% Triton X-100 in PBS after which
650 sections were incubated with primary antibodies (see ***Key Resources Table***) in wash buffer
651 (blocking buffer diluted 10 times in PBS) overnight at 4°C. After washing in PBS, CMCs were
652 incubated at room temperature for 4 hours with rhodamine-labeled phalloidin (1:100, Merck Life
653 Science) and/or Alexa-Fluor-488, -568, or -647-conjugated IgG secondary antibodies (1:500,
654 Thermo Fisher Scientific). Conventional confocal microscopy was performed on a Leica SP8
655 inverted confocal microscope with a 60X oil immersion lens, while STED microscopy was
656 performed on a Leica SP8 STED3X SMD/FCS confocal microscope. Individual images (1024 x
657 1024) were converted to tiff format and merged as pseudocolor RGB images using ImageJ (NIH).
658

Transmission Electron Microscopy (TEM)

For TEM, hearts from cPKOi and control mice 2 and 6 months after TAM induction were excised and fixed in 3.5% glutaraldehyde in 0.15 M sodium cacodylate buffer, pH 7.4, as described (Boncompagni, Rossi, Micaroni, Beznoussenko, et al., 2009; Boncompagni, Rossi, Micaroni, Hamilton, et al., 2009). Small bundles of fibers teased from the papillary muscles were then post-fixed in 2% OsO4 in NaCaCo buffer for 2 hours and block-stained in saturated uranyl acetate. After dehydration, specimens were embedded in an epoxy resin (Epon 812). Ultrathin sections (~50 nm) were cut using a Leica Ultracut R microtome (Leica Microsystem, Austria) with a Diatome diamond knife (DiATOME) and double-stained with uranyl acetate and lead citrate. Sections were viewed in a FP 505 Morgagni Series 268D electron microscope (FEI Company), equipped with a Megaview III digital camera and Soft Imaging System at 60 kV. The ICD fold amplitude was measured at several locations for each ICD on transmission electron micrographs of longitudinally sectioned papillary muscle at a magnification of 11.000x using the TEM Analysis Software. The ICD amplitude was defined as the width of the fold region as indicated in ***Figure 5B***. Sarcomere and I-band lengths were determined on each micrograph in the proximity of the ICD to exclude micrographs presenting shrinkage of the specimens due to fixation and/or longitudinal distortion caused during the cutting of the section.

SDS-PAGE and Western Blot analysis

For Western blot analysis, LV tissue or adult CMCs were homogenized in RIPA buffer containing 50 mM Tris pH 7.5, 150 mM NaCl, 0.5 mM DTT, 1 mM EDTA, 1% (v/v) SDS, 1% (v/v) Triton X-100, 1 mM PMSF, Roche Complete Protease Inhibitor Cocktail (Thermo Fisher Scientific), and Pierce™ Phosphatase Inhibitor Mini Tablets (Thermo Fisher Scientific) using a TissueLyser II (Qiagen). Protein concentration was determined using the Bio-Rad DC™ Protein Assay Kit (Bio-Rad Laboratories) according to the manufacturer's instructions. Western blot analyses were performed using the primary and secondary antibodies listed in the ***Key Resources Table***. The

Immobilon™ Western Chemiluminescent HRP Substrate (Merck Life Science) was used and chemiluminescence was detected on a Chemidoc™ MP System (Bio-Rad Laboratories). Relative protein expression was determined by densitometry using Image Lab, version 6.1.0 software (Bio-Rad Laboratories). GAPDH was used for normalization.

Titin isoform separation and phospho-titin analysis by Western blot analysis

Separation of titin isoforms by SDS-PAGE and Western blot analyses were performed as previously described (Hamdani et al., 2013). Briefly, LV tissue was solubilized in 50 mM Tris-SDS buffer (pH 6.8) containing 8 µg/mL leupeptin (Merck Life Science) and phosphatase inhibitor cocktail (Merck Life Science). SDS-PAGE was performed on 1.8% polyacrylamide/1% agarose gels run at 5 mA for 16 hours, whereafter titin bands were visualized by Coomassie blue staining. Titin isoform ratio was calculated as the densitometric value for titin N2BA over N2B. For determination of total phosphoserine/threonine phosphorylation and site-specific titin phosphorylation, Western blots were performed using anti-phosphoserine/threonine antibody (ECM Biosciences #PP2551; 1:500) as well as titin phosphosite-specific antibodies against pTTN-Ser3991 (N2B region; phosphorylated by PKA and ERK2; 1:500), pTTN-Ser4080 (N2B region; phosphorylated by PKG; 1:500), and pTTN-Ser12742 (PEVK region; phosphorylated by PKCα; 1:500) (Kotter et al., 2013). Densitometry was performed by normalization to total protein content as determined by Coomassie blue staining of each blot.

Statistical analysis

Sample sizes with adequate power to detect statistical differences between groups were determined based on our previous experience and gold standards in the field. The only exclusion criteria were technical failure or death/injury. Data are represented as mean ± standard error of the mean (SEM). Statistical comparisons between two groups were done using the unpaired Student's t-test. Comparisons between multiple groups were performed by one-way or two-way ANOVA with

Šídák's or Tukey's multiple comparisons test, as indicated. The Shapiro-Wilk test was performed to confirm normal distribution in each group and in residuals from a linear regression model, Bartlett's test to check for homogeneity of variance across groups, and Spearman's rank correlation test to confirm heteroscedasticity of residuals. The residuals diagnostic was performed with the DHARMa package, version 0.4.1 in R (R Core Team, 2021). When necessary, data were transformed to meet ANOVA assumptions. For the statistical analyses of echocardiographic parameters over time, a linear mixed model with Tukey's multiple comparisons test was used. The statistical analysis of qRT-PCR data from human biopsies, which did not show equal standard deviation, was performed by Brown-Forsythe and Welch ANOVA with Dunnett's T3 multiple comparisons test. The functional comparisons of sarcomere shortening and Ca^{2+} transients in CMCs were performed using two-level hierarchical testing with Bonferroni correction to eliminate the effects of variations both within cells and between mice (Sikkel et al., 2017). $P < 0.05$ was considered statistically significant. Statistical analysis was performed using Prism 9 (GraphPad) or RStudio, version 1.2.5019 (RStudio Team, 2020) software.

Acknowledgements

We thank Dr. Ju Chen (University of California San Diego, La Jolla CA, USA), who provided advise and support for the generation of *Palld*$^{fl/fl}$ mice, and Marion von Frieling-Salewsky (University of Münster, Münster, Germany) for performing titin gel electrophoresis and Western blot analysis. This work was supported by the Italian Telethon foundation [GGP12282 to M.L.B]; the Italian Ministry of Education, Universities and Research [MiUR PRIN 2010–2011; 2010R8JK2X_006 to MLB]; and the European Union's Horizon 2020 research and innovation program [SILICOFCM; 777204 to CP].

Funding

This work was supported by the Italian Telethon foundation [GGP12282 to M.L.B]; the Italian

737 Ministry of Education, Universities and Research [MiUR PRIN 2010–2011; 2010R8JK2X_006 to
738 MLB]; and the European Union's Horizon 2020 research and innovation program [SILICOFCM;
739 777204 to CP].

740

741 **Competing interests:** The authors declare that no competing interests exist.

References

Abel, E. D., Kaulbach, H. C., Tian, R., Hopkins, J. C., Duffy, J., Doetschman, T., Minnemann, T., Boers, M. E., Hadro, E., Oberste-Berghaus, C., Quist, W., Lowell, B. B., Ingwall, J. S., & Kahn, B. B. (1999). Cardiac hypertrophy with preserved contractile function after selective deletion of GLUT4 from the heart. *J Clin Invest, 104*(12), 1703-1714. DOI: https://doi.org/10.1172/JCI7605

Al Haj, A., Mazur, A. J., Radaszkiewicz, K., Radaszkiewicz, T., Makowiecka, A., Stopschinski, B. E., Schonichen, A., Geyer, M., & Mannherz, H. G. (2015). Distribution of formins in cardiac muscle: FHOD1 is a component of intercalated discs and costameres. *Eur J Cell Biol, 94*(2), 101-113. DOI: https://doi.org/10.1016/j.ejcb.2014.11.003

Bagnall, R. D., Yeates, L., & Semsarian, C. (2010). Analysis of the Z-disc genes PDLIM3 and MYPN in patients with hypertrophic cardiomyopathy. *Int J Cardiol, 145*(3), 601-602. DOI: https://doi.org/10.1016/j.ijcard.2010.08.004

Bang, M. L., Bogomolovas, J., & Chen, J. (2022). Understanding the molecular basis of cardiomyopathy. *Am J Physiol Heart Circ Physiol, 322*(2), H181-h233. DOI: https://doi.org/10.1152/ajpheart.00562.2021

Bang, M. L., Gu, Y., Dalton, N. D., Peterson, K. L., Chien, K. R., & Chen, J. (2014). The muscle ankyrin repeat proteins CARP, Ankrd2, and DARP are not essential for normal cardiac development and function at basal conditions and in response to pressure overload. *PLoS One, 9*(4), e93638. DOI: https://doi.org/10.1371/journal.pone.0093638

Bang, M. L., Mudry, R. E., McElhinny, A. S., Trombitas, K., Geach, A. J., Yamasaki, R., Sorimachi, H., Granzier, H., Gregorio, C. C., & Labeit, S. (2001). Myopalladin, a novel 145-kilodalton sarcomeric protein with multiple roles in Z-disc and I-band protein assemblies. *J Cell Biol, 153*(2), 413-427. DOI: https://doi.org/10.1083/jcb.153.2.413

767 Bennett, P. M. (2012). From myofibril to membrane; the transitional junction at the intercalated
768 disc. *Front Biosci (Landmark Ed), 17*, 1035-1050. DOI: https://doi.org/10.2741/3972
769 Bogomolovas, J., Brohm, K., Celutkiene, J., Balciunaite, G., Bironaite, D., Bukelskiene, V.,
770 Daunoravicus, D., Witt, C. C., Fielitz, J., Grabauskiene, V., & Labeit, S. (2015). Induction
771 of Ankrd1 in Dilated Cardiomyopathy Correlates with the Heart Failure Progression.
772 *Biomed Res Int, 2015*, 273936. DOI: https://doi.org/10.1155/2015/273936
773 Boncompagni, S., Rossi, A. E., Micaroni, M., Beznoussenko, G. V., Polishchuk, R. S., Dirksen, R.
774 T., & Protasi, F. (2009). Mitochondria are linked to calcium stores in striated muscle by
775 developmentally regulated tethering structures. *Molecular biology of the cell, 20*(3), 1058-
776 1067. DOI: https://doi.org/10.1091/mbc.e08-07-0783
777 Boncompagni, S., Rossi, A. E., Micaroni, M., Hamilton, S. L., Dirksen, R. T., Franzini-Armstrong,
778 C., & Protasi, F. (2009). Characterization and temporal development of cores in a mouse
779 model of malignant hyperthermia. *Proceedings of the National Academy of Sciences,*
780 *106*(51), 21996-22001. DOI: https://doi.org/10.1073/pnas.0911496106
781 Borrmann, C. M., Grund, C., Kuhn, C., Hofmann, I., Pieperhoff, S., & Franke, W. W. (2006). The
782 area composita of adhering junctions connecting heart muscle cells of vertebrates. II.
783 Colocalizations of desmosomal and fascia adhaerens molecules in the intercalated disk. *Eur*
784 *J Cell Biol, 85*(6), 469-485. DOI: https://doi.org/10.1016/j.ejcb.2006.02.009
785 Boukhelifa, M., Moza, M., Johansson, T., Rachlin, A., Parast, M., Huttelmaier, S., Roy, P.,
786 Jockusch, B. M., Carpen, O., Karlsson, R., & Otey, C. A. (2006). The proline-rich protein
787 palladin is a binding partner for profilin. *FEBS J, 273*(1), 26-33. DOI:
788 https://doi.org/10.1111/j.1742-4658.2005.05036.x
789 Boukhelifa, M., Parast, M. M., Bear, J. E., Gertler, F. B., & Otey, C. A. (2004). Palladin is a novel
790 binding partner for Ena/VASP family members. *Cell Motil Cytoskeleton, 58*(1), 17-29. DOI:
791 https://doi.org/10.1002/cm.10173

792 Brower, G. L., Gardner, J. D., & Janicki, J. S. (2003). Gender mediated cardiac protection from
793 adverse ventricular remodeling is abolished by ovariectomy. *Mol Cell Biochem, 251*(1-2),
794 89-95.
795 Chen, J. W., Zhou, B., Yu, Q. C., Shin, S. J., Jiao, K., Schneider, M. D., Baldwin, H. S., &
796 Bergelson, J. M. (2006). Cardiomyocyte-specific deletion of the coxsackievirus and
797 adenovirus receptor results in hyperplasia of the embryonic left ventricle and abnormalities
798 of sinuatrial valves. *Circ Res, 98*(7), 923-930. DOI:
799 https://doi.org/10.1161/01.RES.0000218041.41932.e3
800 Ding, Y., Yang, J., Chen, P., Lu, T., Jiao, K., Tester, D. J., Giudicessi, J. R., Jiang, K., Ackerman,
801 M. J., Li, Y., Wang, D. W., Lee, H. C., Wang, D. W., & Xu, X. (2020). Knockout of
802 SORBS2 Protein Disrupts the Structural Integrity of Intercalated Disc and Manifests
803 Features of Arrhythmogenic Cardiomyopathy. *J Am Heart Assoc, 9*(17), e017055. DOI:
804 https://doi.org/10.1161/jaha.119.017055
805 Dixon, R. D., Arneman, D. K., Rachlin, A. S., Sundaresan, N. R., Costello, M. J., Campbell, S. L.,
806 & Otey, C. A. (2008). Palladin is an actin cross-linking protein that uses immunoglobulin-
807 like domains to bind filamentous actin. *J Biol Chem, 283*(10), 6222-6231. DOI:
808 https://doi.org/10.1074/jbc.M707694200
809 Du, X. J. (2004). Gender modulates cardiac phenotype development in genetically modified mice.
810 *Cardiovasc Res, 63*(3), 510-519. DOI: https://doi.org/10.1016/j.cardiores.2004.03.027
811 Duboscq-Bidot, L., Xu, P., Charron, P., Neyroud, N., Dilanian, G., Millaire, A., Bors, V., Komajda,
812 M., & Villard, E. (2008). Mutations in the Z-band protein myopalladin gene and idiopathic
813 dilated cardiomyopathy. *Cardiovasc Res, 77*(1), 118-125. DOI:
814 https://doi.org/10.1093/cvr/cvm015
815 Dwyer, J., Pluess, M., Iskratsch, T., Dos Remedios, C. G., & Ehler, E. (2014). The formin FHOD1
816 in cardiomyocytes. *Anat Rec (Hoboken), 297*(9), 1560-1570. DOI:
817 https://doi.org/10.1002/ar.22984

El-Brolosy, M. A., & Stainier, D. Y. R. (2017). Genetic compensation: A phenomenon in search of mechanisms. *PLoS Genet, 13*(7), e1006780. DOI: https://doi.org/10.1371/journal.pgen.1006780

Endlich, N., Schordan, E., Cohen, C. D., Kretzler, M., Lewko, B., Welsch, T., Kriz, W., Otey, C. A., & Endlich, K. (2009). Palladin is a dynamic actin-associated protein in podocytes. *Kidney Int, 75*(2), 214-226. DOI: https://doi.org/10.1038/ki.2008.486

Filomena, M. C., Yamamoto, D. L., Caremani, M., Kadarla, V. K., Mastrototaro, G., Serio, S., Vydyanath, A., Mutarelli, M., Garofalo, A., Pertici, I., Knoll, R., Nigro, V., Luther, P. K., Lieber, R. L., Beck, M. R., Linari, M., & Bang, M. L. (2020). Myopalladin promotes muscle growth through modulation of the serum response factor pathway. *J Cachexia Sarcopenia Muscle, 11*(1), 169-194. DOI: https://doi.org/10.1002/jcsm.12486

Filomena, M. C., Yamamoto, D. L., Carullo, P., Medvedev, R., Ghisleni, A., Piroddi, N., Scellini, B., Crispino, R., D'Autilia, F., Zhang, J., Felicetta, A., Nemska, S., Serio, S., Tesi, C., Catalucci, D., Linke, W. A., Polishchuk, R., Poggesi, C., Gautel, M., & Bang, M. L. (2021). Myopalladin knockout mice develop cardiac dilation and show a maladaptive response to mechanical pressure overload. *Elife, 10*. DOI: https://doi.org/10.7554/eLife.58313

Franke, W. W., Borrmann, C. M., Grund, C., & Pieperhoff, S. (2006). The area composita of adhering junctions connecting heart muscle cells of vertebrates. I. Molecular definition in intercalated disks of cardiomyocytes by immunoelectron microscopy of desmosomal proteins. *Eur J Cell Biol, 85*(2), 69-82. DOI: https://doi.org/10.1016/j.ejcb.2005.11.003

Gilam, A., Conde, J., Weissglas-Volkov, D., Oliva, N., Friedman, E., Artzi, N., & Shomron, N. (2016). Local microRNA delivery targets Palladin and prevents metastatic breast cancer. *Nat Commun, 7*, 12868. DOI: https://doi.org/10.1038/ncomms12868

Goicoechea, S., Arneman, D., Disanza, A., Garcia-Mata, R., Scita, G., & Otey, C. A. (2006). Palladin binds to Eps8 and enhances the formation of dorsal ruffles and podosomes in

vascular smooth muscle cells. *J Cell Sci, 119*(Pt 16), 3316-3324. DOI: https://doi.org/10.1242/jcs.03076

Goicoechea, S. M., Bednarski, B., Garcia-Mata, R., Prentice-Dunn, H., Kim, H. J., & Otey, C. A. (2009). Palladin contributes to invasive motility in human breast cancer cells. *Oncogene, 28*(4), 587-598. DOI: https://doi.org/10.1038/onc.2008.408

Goicoechea, S. M., Bednarski, B., Stack, C., Cowan, D. W., Volmar, K., Thorne, L., Cukierman, E., Rustgi, A. K., Brentnall, T., Hwang, R. F., McCulloch, C. A., Yeh, J. J., Bentrem, D. J., Hochwald, S. N., Hingorani, S. R., Kim, H. J., & Otey, C. A. (2010). Isoform-specific upregulation of palladin in human and murine pancreas tumors. *PLoS One, 5*(4), e10347. DOI: https://doi.org/10.1371/journal.pone.0010347

Grizzi, F., Fiorino, S., Qehajaj, D., Fornelli, A., Russo, C., de Biase, D., Masetti, M., Mastrangelo, L., Zanello, M., Lombardi, R., Domanico, A., Accogli, E., Tura, A., Mirandola, L., Chiriva-Internati, M., Bresalier, R. S., Jovine, E., Leandri, P., & Di Tommaso, L. (2019). Computer-aided assessment of the extra-cellular matrix during pancreatic carcinogenesis: a pilot study. *J Transl Med, 17*(1), 61. DOI: https://doi.org/10.1186/s12967-019-1817-3

Gurung, R., Yadav, R., Brungardt, J. G., Orlova, A., Egelman, E. H., & Beck, M. R. (2016). Actin polymerization is stimulated by actin cross-linking protein palladin. *Biochem J, 473*(4), 383-396. DOI: https://doi.org/10.1042/BJ20151050

Hamdani, N., Krysiak, J., Kreusser, M. M., Neef, S., Dos Remedios, C. G., Maier, L. S., Kruger, M., Backs, J., & Linke, W. A. (2013). Crucial role for Ca2(+)/calmodulin-dependent protein kinase-II in regulating diastolic stress of normal and failing hearts via titin phosphorylation. *Circ Res, 112*(4), 664-674. DOI: https://doi.org/10.1161/CIRCRESAHA.111.300105

Hirschy, A., Croquelois, A., Perriard, E., Schoenauer, R., Agarkova, I., Hoerstrup, S. P., Taketo, M. M., Pedrazzini, T., Perriard, J. C., & Ehler, E. (2010). Stabilised beta-catenin in postnatal ventricular myocardium leads to dilated cardiomyopathy and premature death. *Basic Res Cardiol, 105*(5), 597-608. DOI: https://doi.org/10.1007/s00395-010-0101-8

869 Jin, L. (2011). The actin associated protein palladin in smooth muscle and in the development of
870 diseases of the cardiovasculature and in cancer. *J Muscle Res Cell Motil, 32*(1), 7-17. DOI:
871 https://doi.org/10.1007/s10974-011-9246-9
872 Jin, L., Gan, Q., Zieba, B. J., Goicoechea, S. M., Owens, G. K., Otey, C. A., & Somlyo, A. V.
873 (2010). The actin associated protein palladin is important for the early smooth muscle cell
874 differentiation. *PLoS One, 5*(9), e12823. DOI: https://doi.org/10.1371/journal.pone.0012823
875 Jin, L., Kern, M. J., Otey, C. A., Wamhoff, B. R., & Somlyo, A. V. (2007). Angiotensin II, focal
876 adhesion kinase, and PRX1 enhance smooth muscle expression of lipoma preferred partner
877 and its newly identified binding partner palladin to promote cell migration. *Circ Res, 100*(6),
878 817-825. DOI: https://doi.org/10.1161/01.RES.0000261351.54147.de
879 Jurmeister, S., Baumann, M., Balwierz, A., Keklikoglou, I., Ward, A., Uhlmann, S., Zhang, J. D.,
880 Wiemann, S., & Sahin, Ö. (2012). MicroRNA-200c represses migration and invasion of
881 breast cancer cells by targeting actin-regulatory proteins FHOD1 and PPM1F. *Mol Cell*
882 *Biol, 32*(3), 633-651. DOI: https://doi.org/10.1128/mcb.06212-11
883 Kanki, H., Suzuki, H., & Itohara, S. (2006). High-efficiency CAG-FLPe deleter mice in C57BL/6J
884 background. *Experimental animals, 55*(2), 137-141. DOI:
885 https://doi.org/10.1538/expanim.55.137.
886 Kempton, A., Cefalu, M., Justice, C., Baich, T., Derbala, M., Canan, B., Janssen, P. M. L., Mohler,
887 P. J., & Smith, S. A. (2018). Altered regulation of cardiac ankyrin repeat protein in heart
888 failure. *Heliyon, 4*(1), e00514. DOI: https://doi.org/10.1016/j.heliyon.2018.e00514
889 Kondo, R. P., Dederko, D. A., Teutsch, C., Chrast, J., Catalucci, D., Chien, K. R., & Giles, W. R.
890 (2006). Comparison of contraction and calcium handling between right and left ventricular
891 myocytes from adult mouse heart: a role for repolarization waveform. *J Physiol, 571*(Pt 1),
892 131-146. DOI: https://doi.org/10.1113/jphysiol.2005.101428

König, N., Raynaud, F., Feane, H., Durand, M., Mestre-Francès, N., Rossel, M., Ouali, A., & Benyamin, Y. (2003). Calpain 3 is expressed in astrocytes of rat and Microcebus brain. *J Chem Neuroanat, 25*(2), 129-136. DOI: https://doi.org/10.1016/s0891-0618(02)00102-3

Kostetskii, I., Li, J., Xiong, Y., Zhou, R., Ferrari, V. A., Patel, V. V., Molkentin, J. D., & Radice, G. L. (2005). Induced deletion of the N-cadherin gene in the heart leads to dissolution of the intercalated disc structure. *Circ Res, 96*(3), 346-354. DOI: https://doi.org/10.1161/01.RES.0000156274.72390.2c

Kotter, S., Gout, L., Von Frieling-Salewsky, M., Muller, A. E., Helling, S., Marcus, K., Dos Remedios, C., Linke, W. A., & Kruger, M. (2013). Differential changes in titin domain phosphorylation increase myofilament stiffness in failing human hearts. *Cardiovasc Res, 99*(4), 648-656. DOI: https://doi.org/10.1093/cvr/cvt144

Kreutziger, K. L., Piroddi, N., McMichael, J. T., Tesi, C., Poggesi, C., & Regnier, M. (2011). Calcium binding kinetics of troponin C strongly modulate cooperative activation and tension kinetics in cardiac muscle. *J Mol Cell Cardiol, 50*(1), 165-174. DOI: https://doi.org/10.1016/j.yjmcc.2010.10.025

Lai, C. F., Bai, S., Uthgenannt, B. A., Halstead, L. R., McLoughlin, P., Schafer, B. W., Chu, P. H., Chen, J., Otey, C. A., Cao, X., & Cheng, S. L. (2006). Four and half lim protein 2 (FHL2) stimulates osteoblast differentiation. *J Bone Miner Res, 21*(1), 17-28. DOI: https://doi.org/10.1359/JBMR.050915

Laure, L., Daniele, N., Suel, L., Marchand, S., Aubert, S., Bourg, N., Roudaut, C., Duguez, S., Bartoli, M., & Richard, I. (2010). A new pathway encompassing calpain 3 and its newly identified substrate cardiac ankyrin repeat protein is involved in the regulation of the nuclear factor-kappaB pathway in skeletal muscle. *FEBS J, 277*(20), 4322-4337. DOI: https://doi.org/10.1111/j.1742-4658.2010.07820.x

Li, C., Liu, F., Liu, S., Pan, H., Du, H., Huang, J., Xie, Y., Li, Y., Zhao, R., & Wei, Y. (2020). Elevated myocardial SORBS2 and the underlying implications in left ventricular

noncompaction cardiomyopathy. *EBioMedicine, 53*, 102695. DOI: https://doi.org/10.1016/j.ebiom.2020.102695

Li, J., Goossens, S., van Hengel, J., Gao, E., Cheng, L., Tyberghein, K., Shang, X., De Rycke, R., van Roy, F., & Radice, G. L. (2012). Loss of αT-catenin alters the hybrid adhering junctions in the heart and leads to dilated cardiomyopathy and ventricular arrhythmia following acute ischemia. *J Cell Sci, 125*(Pt 4), 1058-1067. DOI: https://doi.org/10.1242/jcs.098640

Liotta, L., Lange, S., Maurer, H. C., Olive, K. P., Braren, R., Pfarr, N., Muckenhuber, A., Jesinghaus, M., Weichert, W., Steiger, K., Burger, S., Friess, H., Schmid, R. M., Alguel, H., Jost, P., Ramser, J., Fischer, C., Quante, A. S., Reichert, M., & Quante, M. (2021). PALLD mutation in a European family conveys a stromal predisposition for familial pancreatic cancer. *JCI Insight*. DOI: https://doi.org/10.1172/jci.insight.141532

Loescher, C. M., Hobbach, A. J., & Linke, W. A. (2021). Titin (TTN): from molecule to modifications, mechanics and medical significance. *Cardiovasc Res*. DOI: https://doi.org/10.1093/cvr/cvab328

Luo, H., Liu, X., Wang, F., Huang, Q., Shen, S., Wang, L., Xu, G., Sun, X., Kong, H., Gu, M., Chen, S., Chen, Z., & Wang, Z. (2005). Disruption of palladin results in neural tube closure defects in mice. *Mol Cell Neurosci, 29*(4), 507-515. DOI: https://doi.org/10.1016/j.mcn.2004.12.002

Madrid, R., Gasteier, J. E., Bouchet, J., Schröder, S., Geyer, M., Benichou, S., & Fackler, O. T. (2005). Oligomerization of the diaphanous-related formin FHOD1 requires a coiled-coil motif critical for its cytoskeletal and transcriptional activities. *FEBS Lett, 579*(2), 441-448. DOI: https://doi.org/10.1016/j.febslet.2004.12.009

Mastrototaro, G., Liang, X., Li, X., Carullo, P., Piroddi, N., Tesi, C., Gu, Y., Dalton, N. D., Peterson, K. L., Poggesi, C., Sheikh, F., Chen, J., & Bang, M. L. (2015). Nebulette knockout mice have normal cardiac function, but show Z-line widening and up-regulation of cardiac stress markers. *Cardiovasc Res, 107*(2), 216-225. DOI: https://doi.org/10.1093/cvr/cvv156

945 Meyer, T., Ruppert, V., Ackermann, S., Richter, A., Perrot, A., Sperling, S. R., Posch, M. G.,
946 Maisch, B., & Pankuweit, S. (2013). Novel mutations in the sarcomeric protein myopalladin
947 in patients with dilated cardiomyopathy. *Eur J Hum Genet, 21*(3), 294-300. DOI:
948 https://doi.org/10.1038/ejhg.2012.173
949 Miller, M. K., Bang, M. L., Witt, C. C., Labeit, D., Trombitas, C., Watanabe, K., Granzier, H.,
950 McElhinny, A. S., Gregorio, C. C., & Labeit, S. (2003). The muscle ankyrin repeat proteins:
951 CARP, ankrd2/Arpp and DARP as a family of titin filament-based stress response
952 molecules. *J Mol Biol, 333*(5), 951-964. DOI: https://doi.org/10.1016/j.jmb.2003.09.012
953 Mykkanen, O. M., Gronholm, M., Ronty, M., Lalowski, M., Salmikangas, P., Suila, H., & Carpen,
954 O. (2001). Characterization of human palladin, a microfilament-associated protein. *Mol Biol*
955 *Cell, 12*(10), 3060-3073. DOI: https://doi.org/10.1091/mbc.12.10.3060
956 Nagueh, S. F., Shah, G., Wu, Y., Torre-Amione, G., King, N. M., Lahmers, S., Witt, C. C., Becker,
957 K., Labeit, S., & Granzier, H. L. (2004). Altered titin expression, myocardial stiffness, and
958 left ventricular function in patients with dilated cardiomyopathy. *Circulation, 110*(2), 155-
959 162. DOI: https://doi.org/10.1161/01.CIR.0000135591.37759.AF
960 Norgett, E. E., Hatsell, S. J., Carvajal-Huerta, L., Cabezas, J. C., Common, J., Purkis, P. E.,
961 Whittock, N., Leigh, I. M., Stevens, H. P., & Kelsell, D. P. (2000). Recessive mutation in
962 desmoplakin disrupts desmoplakin-intermediate filament interactions and causes dilated
963 cardiomyopathy, woolly hair and keratoderma. *Hum Mol Genet, 9*(18), 2761-2766. DOI:
964 https://doi.org/10.1093/hmg/9.18.2761
965 Otey, C. A., Dixon, R., Stack, C., & Goicoechea, S. M. (2009). Cytoplasmic Ig-domain proteins:
966 cytoskeletal regulators with a role in human disease. *Cell Motil Cytoskeleton, 66*(8), 618-
967 634. DOI: https://doi.org/10.1002/cm.20385
968 Parast, M. M., & Otey, C. A. (2000). Characterization of palladin, a novel protein localized to stress
969 fibers and cell adhesions. *J Cell Biol, 150*(3), 643-656. DOI:
970 https://doi.org/10.1083/jcb.150.3.643

971 Pashmforoush, M., Pomiès, P., Peterson, K. L., Kubalak, S., Ross, J., Jr., Hefti, A., Aebi, U.,
972 Beckerle, M. C., & Chien, K. R. (2001). Adult mice deficient in actinin-associated LIM-
973 domain protein reveal a developmental pathway for right ventricular cardiomyopathy. *Nat*
974 *Med, 7*(5), 591-597. DOI: https://doi.org/10.1038/87920

975 Pogue-Geile, K. L., Chen, R., Bronner, M. P., Crnogorac-Jurcevic, T., Moyes, K. W., Dowen, S.,
976 Otey, C. A., Crispin, D. A., George, R. D., Whitcomb, D. C., & Brentnall, T. A. (2006).
977 Palladin mutation causes familial pancreatic cancer and suggests a new cancer mechanism.
978 *PLoS Med, 3*(12), e516. DOI: https://doi.org/10.1371/journal.pmed.0030516

979 Purevjav, E., Arimura, T., Augustin, S., Huby, A. C., Takagi, K., Nunoda, S., Kearney, D. L.,
980 Taylor, M. D., Terasaki, F., Bos, J. M., Ommen, S. R., Shibata, H., Takahashi, M., Itoh-
981 Satoh, M., McKenna, W. J., Murphy, R. T., Labeit, S., Yamanaka, Y., Machida, N., Park, J.
982 E., Alexander, P. M., Weintraub, R. G., Kitaura, Y., Ackerman, M. J., Kimura, A., &
983 Towbin, J. A. (2012). Molecular Basis for Clinical Heterogeneity in Inherited
984 Cardiomyopathies Due to Myopalladin Mutations. *Hum Mol Genet, 21*(9), 2039-2053. DOI:
985 https://doi.org/10.1093/hmg/dds022

986 R Core Team (2021). R: A language and environment for statistical computing. *R Foundation for*
987 *Statistical Computing, Vienna, Austria.* URL*:* https://www.R-project.org/

988 Rachlin, A. S., & Otey, C. A. (2006). Identification of palladin isoforms and characterization of an
989 isoform-specific interaction between Lasp-1 and palladin. *J Cell Sci, 119*(Pt 6), 995-1004.
990 DOI: https://doi.org/10.1242/jcs.02825

991 Ronty, M., Taivainen, A., Heiska, L., Otey, C., Ehler, E., Song, W. K., & Carpen, O. (2007).
992 Palladin interacts with SH3 domains of SPIN90 and Src and is required for Src-induced
993 cytoskeletal remodeling. *Exp Cell Res, 313*(12), 2575-2585. DOI:
994 https://doi.org/10.1016/j.yexcr.2007.04.030

995 Ronty, M., Taivainen, A., Moza, M., Kruh, G. D., Ehler, E., & Carpen, O. (2005). Involvement of
996 palladin and alpha-actinin in targeting of the Abl/Arg kinase adaptor ArgBP2 to the actin
997 cytoskeleton. *Exp Cell Res, 310*(1), 88-98. DOI: https://doi.org/10.1016/j.yexcr.2005.06.026
998 Ronty, M., Taivainen, A., Moza, M., Otey, C. A., & Carpen, O. (2004). Molecular analysis of the
999 interaction between palladin and alpha-actinin. *FEBS Lett, 566*(1-3), 30-34. DOI:
1000 https://doi.org/10.1016/j.febslet.2004.04.006
1001 Rstudio Team (2020). RStudio: Integrated Development for R. *RStudio, PBC, Boston, MA, USA*.
1002 URL: http://www.rstudio.com/
1003 Sanematsu, F., Kanai, A., Ushijima, T., Shiraishi, A., Abe, T., Kage, Y., Sumimoto, H., & Takeya,
1004 R. (2019). Fhod1, an actin-organizing formin family protein, is dispensable for cardiac
1005 development and function in mice. *Cytoskeleton (Hoboken), 76*(2), 219-229. DOI:
1006 https://doi.org/10.1002/cm.21523
1007 Schönichen, A., Mannherz, H. G., Behrmann, E., Mazur, A. J., Kühn, S., Silván, U.,
1008 Schoenenberger, C. A., Fackler, O. T., Raunser, S., Dehmelt, L., & Geyer, M. (2013).
1009 FHOD1 is a combined actin filament capping and bundling factor that selectively associates
1010 with actin arcs and stress fibers. *J Cell Sci, 126*(Pt 8), 1891-1901. DOI:
1011 https://doi.org/10.1242/jcs.126706
1012 Sheikh, F., Chen, Y., Liang, X., Hirschy, A., Stenbit, A. E., Gu, Y., Dalton, N. D., Yajima, T., Lu,
1013 Y., Knowlton, K. U., Peterson, K. L., Perriard, J. C., & Chen, J. (2006). alpha-E-catenin
1014 inactivation disrupts the cardiomyocyte adherens junction, resulting in cardiomyopathy and
1015 susceptibility to wall rupture. *Circulation, 114*(10), 1046-1055. DOI:
1016 https://doi.org/10.1161/circulationaha.106.634469
1017 Sikkel, M. B., Francis, D. P., Howard, J., Gordon, F., Rowlands, C., Peters, N. S., Lyon, A. R.,
1018 Harding, S. E., & MacLeod, K. T. (2017). Hierarchical statistical techniques are necessary
1019 to draw reliable conclusions from analysis of isolated cardiomyocyte studies. *Cardiovasc*
1020 *Res, 113*(14), 1743-1752. DOI: https://doi.org/10.1093/cvr/cvx151

1021 Slater, E., Amrillaeva, V., Fendrich, V., Bartsch, D., Earl, J., Vitone, L. J., Neoptolemos, J. P., &
1022 Greenhalf, W. (2007). Palladin mutation causes familial pancreatic cancer: absence in
1023 European families. *PLoS Med,* *4*(4), e164. DOI:
1024 https://doi.org/10.1371/journal.pmed.0040164
1025 Sohal, D. S., Nghiem, M., Crackower, M. A., Witt, S. A., Kimball, T. R., Tymitz, K. M., Penninger,
1026 J. M., & Molkentin, J. D. (2001). Temporally regulated and tissue-specific gene
1027 manipulations in the adult and embryonic heart using a tamoxifen-inducible Cre protein.
1028 *Circ Res, 89*(1), 20-25. DOI: https://doi.org/10.1161/hh1301.092687
1029 Sweet, M. E., Cocciolo, A., Slavov, D., Jones, K. L., Sweet, J. R., Graw, S. L., Reece, T. B.,
1030 Ambardekar, A. V., Bristow, M. R., Mestroni, L., & Taylor, M. R. G. (2018). Transcriptome
1031 analysis of human heart failure reveals dysregulated cell adhesion in dilated cardiomyopathy
1032 and activated immune pathways in ischemic heart failure. *BMC Genomics, 19*(1), 812. DOI:
1033 https://doi.org/10.1186/s12864-018-5213-9
1034 Takeya, R., & Sumimoto, H. (2003). Fhos, a mammalian formin, directly binds to F-actin via a
1035 region N-terminal to the FH1 domain and forms a homotypic complex via the FH2 domain
1036 to promote actin fiber formation. *J Cell Sci, 116*(Pt 22), 4567-4575. DOI:
1037 https://doi.org/10.1242/jcs.00769
1038 Tanaka, N., Dalton, N., Mao, L., Rockman, H. A., Peterson, K. L., Gottshall, K. R., Hunter, J. J.,
1039 Chien, K. R., & Ross, J. (1996). Transthoracic echocardiography in models of cardiac
1040 disease in the mouse. *Circulation,* *94*(5), 1109-1117. DOI:
1041 https://doi.org/10.1161/01.cir.94.5.1109
1042 Vermij, S. H., Abriel, H., & van Veen, T. A. (2017). Refining the molecular organization of the
1043 cardiac intercalated disc. *Cardiovasc Res,* *113*(3), 259-275. DOI:
1044 https://doi.org/10.1093/cvr/cvw259
1045 von Nandelstadh, P., Gucciardo, E., Lohi, J., Li, R., Sugiyama, N., Carpen, O., & Lehti, K. (2014).
1046 Actin-associated protein palladin promotes tumor cell invasion by linking extracellular

matrix degradation to cell cytoskeleton. *Mol Biol Cell, 25*(17), 2556-2570. DOI: https://doi.org/10.1091/mbc.E13-11-0667

von Nandelstadh, P., Ismail, M., Gardin, C., Suila, H., Zara, I., Belgrano, A., Valle, G., Carpen, O., & Faulkner, G. (2009). A class III PDZ binding motif in the myotilin and FATZ families binds enigma family proteins: a common link for Z-disc myopathies. *Mol Cell Biol, 29*(3), 822-834. DOI: https://doi.org/10.1128/MCB.01454-08

Wang, H. V., & Moser, M. (2008). Comparative expression analysis of the murine palladin isoforms. *Dev Dyn, 237*(11), 3342-3351. DOI: https://doi.org/10.1002/dvdy.21755

Wilson, A. J., Schoenauer, R., Ehler, E., Agarkova, I., & Bennett, P. M. (2014). Cardiomyocyte growth and sarcomerogenesis at the intercalated disc. *Cell Mol Life Sci, 71*(1), 165-181. DOI: https://doi.org/10.1007/s00018-013-1374-5

Yamamoto, D. L., Vitiello, C., Zhang, J., Gokhin, D. S., Castaldi, A., Coulis, G., Piaser, F., Filomena, M. C., Eggenhuizen, P. J., Kunderfranco, P., Camerini, S., Takano, K., Endo, T., Crescenzi, M., Luther, P. K., Lieber, R. L., Chen, J., & Bang, M. L. (2013). The nebulin SH3 domain is dispensable for normal skeletal muscle structure but is required for effective active load bearing in mouse. *J Cell Sci, 126*(Pt 23), 5477-5489. DOI: https://doi.org/10.1242/jcs.137026

Yang, K. C., Yamada, K. A., Patel, A. Y., Topkara, V. K., George, I., Cheema, F. H., Ewald, G. A., Mann, D. L., & Nerbonne, J. M. (2014). Deep RNA sequencing reveals dynamic regulation of myocardial noncoding RNAs in failing human heart and remodeling with mechanical circulatory support. *Circulation, 129*(9), 1009-1021. DOI: https://doi.org/10.1161/CIRCULATIONAHA.113.003863

Young, P., Ferguson, C., Banuelos, S., & Gautel, M. (1998). Molecular structure of the sarcomeric Z-disk: two types of titin interactions lead to an asymmetrical sorting of alpha-actinin. *Embo J, 17*(6), 1614-1624. DOI: https://doi.org/10.1093/emboj/17.6.1614

1072 Zemljic-Harpf, A. E., Miller, J. C., Henderson, S. A., Wright, A. T., Manso, A. M., Elsherif, L.,
1073 Dalton, N. D., Thor, A. K., Perkins, G. A., McCulloch, A. D., & Ross, R. S. (2007).
1074 Cardiac-myocyte-specific excision of the vinculin gene disrupts cellular junctions, causing
1075 sudden death or dilated cardiomyopathy. *Mol Cell Biol, 27*(21), 7522-7537. DOI:
1076 https://doi.org/10.1128/MCB.00728-07
1077 Zhou, Q., Chu, P. H., Huang, C., Cheng, C. F., Martone, M. E., Knoll, G., Shelton, G. D., Evans, S.,
1078 & Chen, J. (2001). Ablation of Cypher, a PDZ-LIM domain Z-line protein, causes a severe
1079 form of congenital myopathy. *J Cell Biol, 155*(4), 605-612. DOI:
1080 https://doi.org/10.1083/jcb.200107092
1081 Zolk, O., Frohme, M., Maurer, A., Kluxen, F. W., Hentsch, B., Zubakov, D., Hoheisel, J. D.,
1082 Zucker, I. H., Pepe, S., & Eschenhagen, T. (2002). Cardiac ankyrin repeat protein, a
1083 negative regulator of cardiac gene expression, is augmented in human heart failure. *Biochem*
1084 *Biophys Res Commun, 293*(5), 1377-1382. DOI: https://doi.org/10.1016/S0006-
1085 291X(02)00387-X
1086

Table

Table 1. Tension generation and relaxation in ventricular myofibrils from inducible cardiomyocyte-specific palladin knockout (cPKOi) mice and control male mice 2 months after tamoxifen (TAM) induction.

	Resting conditions		Tension generation		Relaxation		
					Slow Phase		Fast Phase
Myofibril batch	SL (μm)	RT (mN mm^{-2})	P_0 (mN mm^{-2})	k_{ACT} (s^{-1})	Duration (ms)	k_{REL} (s^{-1})	k_{REL} (s^{-1})
***Palld*$^{fl/fl}$; TAM**	2.13±0.02 (30)	8.65±1.03 (30)	138±7 (30)	4.98±0.30 (30)	78.2±3.9 (25)	2.02±0.22 (25)	20.8±2.2 (29)
MRM$^{+/0}$ TAM	2.13±0.02 (33)	9.01±1.02 (33)	129±9 (33)	4.91±0.28 (31)	74.7±3.5 (27)	1.54±0.19 (27)	28.4±2.8 (27)
***Palld*$^{fl/fl}$; MRM$^{+/0}$ TAM**	2.14±0.02 (23)	9.67±1.81 (23)	**111±8*** **(23)**	4.83±0.43 (23)	86.5±4.8 (22)	1.86±0.19 (22)	21.5±1.2 (22)

All data are represented as mean ± standard error of the mean (SEM). Numbers in parentheses are number of myofibrils. SL, sarcomere length, RT, resting tension, P_0, maximum isometric tension; k_{ACT}, rate constant of tension rise following step-wise pCa decrease (8.0→4.5) by fast solution switching. Full tension relaxation kinetics were characterized by the duration and rate constant of tension decay of the isometric slow relaxation phase (slow k_{REL}) and the rate constant of the fast relaxation phase (fast k_{REL}). *$P < 0.05$ *vs.* *Palld*$^{fl/fl}$; TAM; one-way analysis of variance (ANOVA) with Šídák's multiple comparisons test.

The online version of this article includes the following figure supplement for Table 1:

Figure supplement 1. Sarcomere-length tension relationship in cardiac myofibrils from the left ventricle of inducible cardiomyocyte-specific palladin knockout (cPKOi) and control male mice 2 months after tamoxifen (TAM) induction.

Figure legends

Figure 1. Palladin (PALLD) binds to cardiac ankyrin repeat protein (CARP/Ankrd1) and formin homology 2 domain containing 1 (FHOD1) and is localized in the Z-line, I-band, intercalated disc (ICD), and nucleus in cardiomyocytes (CMCs). (**A**) Schematic representation of the domain structure of PALLD. Proline-rich regions are shown in yellow. Binding sites for known and novel interaction partners are shown with the ones

in common with myopalladin (MYPN) in red. In a yeast two-hybrid screening, the N-terminal region of PALLD, comprising 2 Ig domains, was found to bind to CARP and FHOD1, as illustrated. The interacting region in FHOD1 was narrowed down to a region within the C-terminal region of FHOD1 (residue 965-1052), as indicated. GBD, GTPase-binding domain; DID, diaphanous inhibitory domain; FH1, formin homology 1 domain; FH2, formin homology 2 domain; DAD, diaphanous autoregulatory domain. (**B**) Confirmation of PALLD-CARP and PALLD-FHOD1 interactions in NanoBRET protein interaction assays with CARP-NanoLuc or FHOD1-NanoLuc as donor and fluorescently labeled PALLD-HaloTag as acceptor. Data are represented as mean ± standard error of the mean (SEM) (n = 3-4). **P < 0.01; Student's t-test. (**C**) Immunofluorescence analysis of sectioned heart by STED microscopy, showing localization of both PALLD and CARP in the sarcomeric I-band. (**D**) Confocal fluorescence microscopy showing the presence of PALLD in the nucleus of CMCs. Both the PALLD 622 antibody and the PALLD Proteintech antibody showed nuclear localization of PALLD in most CMCs (an example of a CMC without nuclear staining for PALLD is shown on the bottom), while the PALLD 4D10 antibody did not stain the nucleus. Nuclei are visualized by DAPI (blue). (**E**) Confocal fluorescence microscopy of sectioned heart, showing colocalization of PALLD and FHOD1 at the ICD and the Z-line. (**F**) Confocal fluorescence microscopy showing colocalization of PALLD and Sorbin And SH3 Domain Containing 2 (SORBS2) at the ICD in CMCs.

The online version of this article includes the following source data and figure supplements for figure 1:

Source data 1. Confirmation of PALLD-CARP and PALLD-FHOD1 interactions in NanoBRET protein interaction assays.

Figure supplement 1. Yeast-two hybrid assays showing the interaction of the N-terminal region of palladin (PALLD) with cardiac ankyrin repeat protein (CARP/Ankrd1) and formin homology 2 domain containing 1 (FHOD1).

Figure supplement 2. Confocal fluorescence microscopy showing the presence of palladin (PALLD) in the nucleus of cardiomyocytes both from wild-type mice and cardiac ankyrin repeat protein (CARP/Ankrd1) knockout (CKO) mice.

Figure 2. Echocardiographic and histological analyses of cardiomyocyte-specific palladin (cPKO) mice, and cPKO and myopalladin (MYPN) double knockout (cPKO/MKO dKO) mice. (**A**) Quantitative real-time PCR (qRT-PCR) for transcripts encoding the most common PALLD isoform on left ventricular (LV) RNA from

8-week-old cPKO (*Palld*$^{fl/fl}$;Cre$^{+/0}$) and control (*Palld*$^{fl/fl}$) male mice (n = 3 biological replicates and 3 technical replicates per group). ***$P < 0.001$; two-way analysis of variance (ANOVA) with Šidák's multiple comparison test. (**B**) Western blot analysis for PALLD (PALLD 622 antibody) on LV lysate from cPKO and control male mice. (**C**) Densitometric analysis for the 90 kDa PALLD isoform using GAPDH for normalization (n = 4-6 per group). ***$P < 0.001$; Student's t-test. (**D**) Echocardiography analyses of cPKO and control male mice under basal conditions and 1, 2, and 4 weeks after transaortic constriction (TAC). Pressure gradient > 70 mmHg. LVID, left ventricular inner diameter; LVPW, left ventricular posterior wall thickness; IVS, interventricular septum thickness; FS, fractional shortening; EF, ejection fraction; d, diastole; s, systole (n = 4-14 per group). *$P < 0.05$; **$P < 0.01$; linear mixed model with Tukey's multiple comparisons test. (**E**) Hematoxylin and eosin (left, middle) and Picro Sirius Red (right) stainings of sections of whole hearts and areas of the LV outer wall from cPKO and control male mice 4 weeks after TAC. (**F**) Percent area of interstitial fibrosis in the LV (n = 3 per group). No statistical difference by one-way ANOVA with Tukey's multiple comparisons test. (**G**) Echocardiographic analysis of cPKO/MKO dKO *vs.* single KO and control male mice at 2 and 4 months (M) of age. See (**D**) for abbreviations (n = 6-42 per group). *$P <$ 0.05; **$P < 0.01$; ***$P < 0.001$; linear mixed model with Tukey's multiple comparisons test. All data are represented as mean ± standard error of the mean (SEM).

The online version of this article includes the following source data and figure supplements for figure 2:

Source data 1. Quantitative real-time PCR (qRT-PCR) and densitometry of Western blots on cardiomyocyte-specific palladin (cPKO) and control male mice.

Source data 2. Uncropped Western blots for Figure 2B.

Source data 3. Echocardiographic parameters of 3- and 6-month-old cardiomyocyte-specific palladin knockout (cPKO) male mice compared to controls under basal conditions.

Source data 4. Echocardiographic analysis on 3- and 6-month-old cardiomyocyte-specific palladin (cPKO) and control male mice.

Source data 5. Echocardiographic parameters of 8-week-old cardiomyocyte-specific palladin knockout (cPKO) male mice compared to controls before and 4 weeks after mechanical pressure overload induced by transaortic constriction (TAC).

Source data 6. Echocardiographic analysis on cardiomyocyte-specific palladin (cPKO) and control male mice subjected to transaortic constriction (TAC) or SHAM.

1166 **Source data 7:** Measurements of fibrotic area in the left ventricle of cardiomyocyte-specific palladin
1167 (cPKO) and control male mice.
1168 **Source data 8.** Echocardiographic parameters of 3- and 6-month-old cardiomyocyte-specific palladin and
1169 myopalladin double knockout (cPKO/MKO dKO) mice subjected to transaortic constriction (TAC) or
1170 SHAM.
1171 **Source data 9.** Echocardiographic analysis on cardiomyocyte-specific palladin (cPKO) and myopalladin
1172 (MYPN) double knockout and control male mice subjected to transaortic constriction (TAC) or SHAM.
1173 **Figure supplement 1.** Generation of *Palld* floxed mice.
1174 **Figure supplement 2.** Echocardiographic and histological analyses of cardiomyocyte-specific palladin
1175 knockout (cPKO) male mice.
1176

1177 **Figure 3.** Echocardiographic and functional analyses of inducible cardiomyocyte-specific palladin knockout
1178 (cPKOi) mice. (**A**) Quantitative real-time PCR (qRT-PCR) for transcripts encoding the most common
1179 palladin (PALLD) isoforms on left ventricular (LV) RNA from cPKOi ($Palld^{fl/fl}$;$MCM^{+/0}$ TAM) and control
1180 ($Palld^{fl/fl}$ TAM) mice 8 weeks after tamoxifen (TAM) induction (n = 4 per group). ***P < 0.001; linear
1181 mixed model with Tukey's multiple comparisons test. (**B**) Western blot analysis for PALLD (PALLD 622
1182 antibody) on adult cardiomyocytes (CMCs) from cPKOi and control mice 8 week after TAM induction. (**C**)
1183 Densitometric analysis for the 90 kDa PALLD isoform using GAPDH for normalization (n = 6-7). ***P <
1184 0.001; Student's t-test. (**D**) Echocardiographic analysis of cPKOi and control male mice 0, 8, and 24 weeks
1185 after TAM induction. See Fig 2A for abbreviations. RWT, relative wall thickness ((LVPWd +
1186 IVSd)/LVIDd); HW, heart weight, BW, body weight (n = 4-44 per group). *P < 0.05; **P < 0.01; ***P <
1187 0.001; linear mixed model with Tukey's multiple comparisons test. (**E**) Representative echocardiographic
1188 short-axis M-mode images of hearts from cPKOi and control mice 24 weeks after TAM induction. (**F**)
1189 IonOptix analysis of ventricular CMC contractility and Ca^{2+} transients in cPKOi male mice *vs*. control mice 3
1190 months after TAM induction. Top, Sarcomere shortening, time to 90% peak, and time to 50% relaxation (n =
1191 33 cells from 4 $Palld^{fl/fl}$ TAM mice, n = 34 cells from 5 $MCM^{+/0}$ TAM mice, and n = 52 cells from 6
1192 $Palld^{fl/fl}$;$MCM^{+/0}$ TAM mice). Bottom, amplitude of Ca^{2+} transient, time to 90% peak of Ca^{2+} transient, and
1193 time to 50% decay of Ca^{2+} transient (n = 39 cells from 4 $Palld^{fl/fl}$ TAM mice, n = 18 cells from 3 $MCM^{+/0}$

TAM mice, and n = 58 cells from 6 *Palld*$^{fl/fl}$;MCM$^{+/0}$ TAM mice). *P < 0.05; **P < 0.01; ***P < 0.001; two-level hierarchical testing with Bonferroni correction (Sikkel et al., 2017). All data are represented as mean ± standard error of the mean (SEM).

The online version of this article includes the following source data for figure 3:

Source data 1. Quantitative real-time PCR (qRT-PCR) and densitometry of Western blots on inducible cardiomyocyte-specific palladin (cPKOi) and control male mice.

Source data 2. Uncropped Western blots for Figure 3B.

Source data 3. Echocardiographic parameters of inducible cardiomyocyte-specific palladin knockout (cPKOi) male mice compared to controls 2 and 6 months after tamoxifen (TAM) induction.

Source data 4. Echocardiographic analysis on inducible cardiomyocyte-specific palladin (cPKOi) and control male mice 2 and 6 months after tamoxifen (TAM) induction.

Source data 5. Heart weight to body weight ratio (HW/BW) measurements on inducible cardiomyocyte-specific palladin (cPKOi) and control male mice 2 and 6 months after tamoxifen (TAM) induction.

Source data 6. Analysis of sarcomere shortening and Ca^{2+} transients in cardiomyocytes from inducible cardiomyocyte-specific palladin (cPKOi) and control male mice.

Figure 4. Histological and molecular analyses of cardiomyocyte-specific palladin knockout (cPKOi) mice. (**A**) Hematoxylin and eosin (top, middle) and Picro Sirius Red (bottom) stainings of sections of whole hearts and areas of the left ventricular (LV) outer wall from cPKOi and control male mice 6 months after tamoxifen (TAM) induction. (**B**) Percent area of interstitial fibrosis in the LV (n = 3 per group). **P < 0.01; one-way analysis of variance (ANOVA) with Tukey's multiple comparisons test. (**C**−**E**) Left, frequency distributions of cardiomyocyte (CMC) size (n = 830 CMCs from 3 *Palld*$^{fl/fl}$ mice and 1079 CMCs from 3 *Palld*$^{fl/fl}$;MCM$^{+/0}$ TAM mice) (**C**), length (n = 877 CMCs from 3 *Palld*$^{fl/fl}$ mice and 1576 CMCs from 3 *Palld*$^{fl/fl}$;MCM$^{+/0}$ TAM mice) (**D**), and width (n = 842 CMCs from 3 *Palld*$^{fl/fl}$ mice and 1565 CMCs from 3 *Palld*$^{fl/fl}$;MCM$^{+/0}$ TAM mice) (**E**) in cPKOi and control male mice 3 months after TAM induction. Right, Average CMC size (**C**), length (**D**), and width (**E**) in the same mice. *P < 0.05; ***P < 0.001; Student's t-test. (**F**) Quantitative real-time PCR (qRT-PCR) analysis on LV RNA from cPKOi and control mice 6 months after TAM induction (n = 4-5). *Gapdh* was used for normalization *P < 0.05; **P < 0.01; ***P < 0.001; one-way ANOVA with Tukey's multiple comparisons test. All data are represented as mean ± standard error of the mean (SEM).

The online version of this article includes the following source data and figure supplements for figure 4:

Source data 1. Cardiomyocyte (CMC) size, length, and width measurements in inducible cardiomyocyte-specific palladin (cPKOi) and control male mice 3 months after tamoxifen (TAM) induction.

Source data 2. Measurements of fibrotic area in the left ventricle of inducible cardiomyocyte-specific palladin (cPKOi) and control male mice 6 months after tamoxifen (TAM) induction.

Source data 3. Raw data for quantitative real-time PCR (qRT-PCR) on inducible cardiomyocyte-specific palladin (cPKOi) and control male mice 6 months after tamoxifen (TAM) induction.

Figure supplement 1. Quantitative real-time PCR (qRT-PCR) analysis on left ventricle from inducible cardiomyocyte-specific palladin knockout (cPKOi) male mice compared to controls 6 months after tamoxifen (TAM) induction.

Figure 5. Transmission electron microscopy (TEM) analysis of papillary muscles from inducible cardiomyocyte-specific palladin knockout (cPKOi) and control mice. (**A**) Representative electron micrographs of papillary muscles from control (*Palld*$^{fl/fl}$ TAM) and cPKOi (*Palld*$^{fl/fl}$;MCM$^{+/0}$ TAM) male mice 2 months and 6 months after tamoxifen (TAM) induction. Black arrows indicate intercalated discs (ICDs). (**B**) Representative electron micrographs of ICD ultrastructure from 6-month-old control and cPKOi mice. Dashed black lines indicate ICD regions. (**C**, **D**) ICD fold amplitude frequency distribution (left) and average (right) in control and cPKOi samples 2 months (n = 147 measurements on 20 ICDs from 2 *Palld*$^{fl/fl}$ mice and 279 measurements on 33 ICDs from 2 *Palld*$^{fl/fl}$;MCM$^{+/0}$ TAM mice) (**C**) and 6 months (n = 236 measurements on 30 ICDs from 2 *Palld*$^{fl/fl}$ mice and 420 measurements on 48 ICDs from 2 *Palld*$^{fl/fl}$;MCM$^{+/0}$ TAM mice) (**D**) after TAM induction. Data are represented as mean ± standard error of the mean (SEM). ***P < 0.001; Welch's t-test. (**E**) Representative electron micrographs of ICDs from control and cPKOi mice 2 and 6 months after TAM induction. Asterisks show thick filaments in abnormal fold regions. (**F**) Electron micrographs showing altered sarcomeric regions (large black arrows) in the proximity of high-amplitude ICDs in papillary muscles from 6-month-old cPKOi mice. White arrows point to jagged Z-lines. Asterisks highlight groups of vesicles. The online version of this article includes the following source data for figure 5:

Source data 1. Intercalated disc (ICD) fold amplitude measurements in inducible cardiomyocyte-specific palladin (cPKOi) and control male mice 2 and 6 months after tamoxifen (TAM) induction.

Figure 6. Molecular analyses on inducible cardiomyocyte-specific palladin knockout (cPKOi) mice and human cardiomyopathy patients. (**A**) Western blot analyses for intercalated disc (ICD) proteins on left ventricular (LV) lysate from cPKOi mice compared to control male mice 2 months after TAM induction. Representative blots are shown. GAPDH was used as loading control. (**B**) Densitometric analysis of blots in (**A**) using GAPDH for normalization (n = 3-4 per group). *$P < 0.05$, one-way analysis of variance (ANOVA) with Tukey's multiple comparisons test. (**C**) Quantitative real-time PCR (qRT-PCR) analysis for *MYPN*, *PALLD* and *ANKRD1* on LV biopsies from ischemic cardiomyopathy (ICM) (n = 8) and dilated cardiomyopathy (DCM) (n = 8) male patients *vs.* healthy control (Ctrl) hearts (n = 5). *HPRT* was used for normalization. *$P < 0.05$, **$P < 0.01$; Brown-Forsythe and Welch ANOVA with Dunnett's T3 multiple comparisons test. All data are represented as mean ± standard error of the mean (SEM).

The online version of this article includes the following source data and figure supplements for figure 6:

Source data 1. Uncropped Western blots for Figure 6A.

Source data 2. Densitometry on Western blots on inducible cardiomyocyte-specific palladin (cPKOi) and control male mice 2 months after tamoxifen (TAM) induction.

Source data 3. Quantitative real-time PCR (qRT-PCR) analysis on left ventricular biopsies from patients with dilated (DCM) and ischemic (ICM) cardiomyopathy *vs*. healthy control (Ctrl) hearts.

Source data 4. Uncropped Western blots for Figure 6–figure supplement 3.

Source data 5. Uncropped Western blots for Figure 6–figure supplement 4.

Figure supplement 1. Immunofluorescence stainings for intercalated disc proteins of cardiomyocytes from inducible cardiomyocyte-specific palladin knockout (cPKOi) and control male mice 4 months after tamoxifen (TAM) induction. Nuclei are visualized by DAPI (blue).

Figure supplement 2. Immunofluorescence stainings of cardiomyocytes for palladin (PALLD) interacting proteins from inducible cardiomyocyte-specific palladin knockout (cPKOi) and control male mice 4 months after tamoxifen (TAM) induction. Nuclei are visualized by DAPI (blue).

Figure supplement 3. Western blot analysis for palladin (PALLD) interacting proteins and proteins involved in cardiac signaling pathways on left ventricular lysate from inducible cardiomyocyte-specific palladin knockout (cPKOi) and control male mice 2 months after tamoxifen (TAM) induction. GAPDH was used as loading control. No differences were found.

Figure supplement 4. Titin isoform expression and phosphorylation in the left ventricular of inducible cardiomyocyte-specific palladin knockout (cPKOi) and control male mice 2 months after tamoxifen (TAM) induction.

Figure supplement 5. Patient characteristics.

Supplementary file 1. Oligos used for quantitative real-time PCR (qRT-PCR) and clonings.

Figure supplement legends

Figure 1–figure supplement 1. Yeast-two hybrid assays showing the interaction of the N-terminal region of palladin (PALLD) with cardiac ankyrin repeat protein (CARP/Ankrd1) and formin homology 2 domain containing 1 (FHOD1). (**A**) Culture plate with different combinations of Y2H cotransformations to narrow down the interaction size between PALLD and CARP as indicated in the table. PALLD's N-terminal region binds to CARP. (**B**) Culture plate with different combinations of Y2H cotransformations to narrow down the interaction size between PALLD and FHOD1 as indicated in the table. FHOD1 residue 965-1052 is sufficient for binding to the N-terminal region of both PALLD and its homologue MYPN.

Figure 1–figure supplement 2. Confocal fluorescence microscopy showing the presence of palladin (PALLD) in the nucleus of cardiomyocytes both from wild-type (WT) mice and cardiac ankyrin repeat protein (CARP/Ankrd1) knockout (CKO) mice.

Figure 2–figure supplement 1. Generation of *Palld* floxed mice. (**A**) Targeting strategy for the generation of *Palld* floxed mice containing LoxP sites flanking exon 15. A restriction map of the relevant genomic region of *Palld* is shown on the top, the targeting construct is shown in the middle, and the mutated locus after recombination is shown at the bottom. Arrowheads indicate loxP sites and black boxes indicate Flpase Recognition Target (FLP) sites. Neo, neomycin resistance gene; DTA, diptheria toxin A fragment gene. (**B**) Detection of wild-type (WT) and targeted alleles by Southern blot analysis following digestion with EcoRV using the probe shown in A. (**C**) Genotyping of WT and *Palld* floxed mice after removal of the neo cassette using *Palld*-specific primers. All data are represented as mean ± standard error of the mean (SEM).

Figure 2–figure supplement 2. Echocardiographic and histological analyses of cardiomyocyte-specific palladin knockout (cPKO) male mice. (**A**) Echocardiographic analysis of cPKO and control male mice at 3 and 6 months (M) of age. LVID, left ventricular inner diameter; LVPW, left ventricular posterior wall thickness; IVS, interventricular septum thickness; FS, fractional shortening; EF, ejection fraction; d, diastole; s, systole (n = 7-17 per group). *$P < 0.05$; LMM with Tukey's multiple comparisons test. (**B**) Hematoxylin and eosin (top, middle) and Picro Sirius Red (bottom) stainings of sections of whole hearts and areas of the left ventricular (LV) outer wall from 6-month-old cPKO and control male mice. (**C**) Percent area of interstitial fibrosis in the LV (n = 3-7 per group). No statistical difference by one-way analysis of variance (ANOVA) with Tukey' multiple comparisons test. All data are represented as mean ± standard error of the mean (SEM).

Figure 4–figure supplement 1. Quantitative real-time PCR (qRT-PCR) analysis on left ventricle from inducible cardiomyocyte-specific palladin knockout (cPKOi) male mice compared to controls 6 months after tamoxifen (TAM) induction.

Figure 6–figure supplement 1. Immunofluorescence stainings for intercalated disc proteins of cardiomyocytes from inducible cardiomyocyte-specific palladin knockout (cPKOi) and control male mice 4 months after tamoxifen (TAM) induction. Nuclei are visualized by DAPI (blue).

Figure 6–figure supplement 2. Immunofluorescence stainings of cardiomyocytes for palladin (PALLD) interacting proteins from inducible cardiomyocyte-specific palladin knockout (cPKOi) and control male mice 4 months after tamoxifen (TAM) induction. Nuclei are visualized by DAPI (blue).

Figure 6–figure supplement 3. Western blot analysis for palladin (PALLD) interacting proteins and proteins involved in cardiac signaling pathways on left ventricular lysate from inducible cardiomyocyte-specific palladin knockout (cPKOi) and control male mice 2 months after tamoxifen (TAM) induction. GAPDH was used as loading control. No differences were found.

Figure 6–figure supplement 4. Titin isoform expression and phosphorylation in the left ventricular of inducible cardiomyocyte-specific palladin knockout (cPKOi) and control male mice 2 months after tamoxifen (TAM) induction. (**A**) SDS-PAGE and Coomassie blue staining for titin (TTN) N2BA and N2B isoforms as well as Western blot analyses using anti-phosphoserine/threonine antibody (pTTN-Ser/Thr) and titin phosphosite-specific antibodies against pTTN-Ser3991 (corresponding to human pTTN-Ser4010 in the N2Bus region), pTTN-Ser4080 (corresponding to human pTTN-Ser4099 in the N2Bus region), and pTTN-Ser12742 (corresponding to human pTTN-Ser11878 in the PEVK region). (**B**) Densitometric analysis of blots in (**A**) for titin (TTN) N2BA/N2B isoform ratio as well as titin serine/threonine phosphorylation and site-specific titin phosphorylation. Normalization was performed to total protein content as determined by Coomassie blue staining of each blot (n = 3 per group). No statistical differences by unpaired Student's t-test. All data are represented as mean ± SEM.

Figure 6–figure supplement 5. Patient characteristics.

Table 1–figure supplement 1. Sarcomere-length tension relationship in cardiac myofibrils from the left ventricle of inducible cardiomyocyte-specific palladin knockout (cPKOi) and control male mice 2 months after tamoxifen (TAM) induction. Each data point is represented as mean ± standard error of the mean (SEM) from 4-12 myofibrils from 3 *Palld*$^{fl/fl}$ TAM mice, from 11-19 myofibrils from 3 MCM$^{+/0}$ TAM mice and from 5-15 myofibrils from 3 *Palld*$^{fl/fl}$;MCM$^{+/0}$ TAM mice.

Supplementary file 1. Oligos used for quantitative real-time PCR (qRT-PCR) and clonings.

Source data files

Figure 1–Source data 1. Confirmation of PALLD-CARP and PALLD-FHOD1 interactions in NanoBRET protein interaction assays.

Figure 2–Source data 1. Quantitative real-time PCR (qRT-PCR) and densitometry of Western blots on cardiomyocyte-specific palladin (cPKO) and control male mice.

Figure 2–Source data 2. Uncropped Western blots for Figure 2B.

Figure 2–Source data 3. Echocardiographic parameters of 3- and 6-month-old cardiomyocyte-specific palladin knockout (cPKO) male mice compared to controls under basal conditions.

Figure 2–Source data 4. Echocardiographic analysis on 3- and 6-month-old cardiomyocyte-specific palladin (cPKO) and control male mice.

Figure 2–Source data 5. Echocardiographic parameters of 8-week-old cardiomyocyte-specific palladin knockout (cPKO) male mice compared to controls before and 4 weeks after mechanical pressure overload induced by transaortic constriction (TAC).

Figure 2–Source data 6. Echocardiographic analysis on cardiomyocyte-specific palladin (cPKO) and control male mice subjected to transaortic constriction (TAC) or SHAM.

Figure 2–Source data 7: Measurements of fibrotic area in the left ventricle of cardiomyocyte-specific palladin (cPKO) and control male mice.

Figure 2–Source data 8. Echocardiographic parameters of 3- and 6-month-old cardiomyocyte-specific palladin and myopalladin double knockout (cPKO/MKO dKO) mice subjected to transaortic constriction (TAC) or SHAM.

Figure 2–Source data 9. Echocardiographic analysis on cardiomyocyte-specific palladin (cPKO) and myopalladin (MYPN) double knockout and control male mice subjected to transaortic constriction (TAC) or SHAM.

Figure 3–Source data 1. Quantitative real-time PCR (qRT-PCR) and densitometry of Western blots on inducible cardiomyocyte-specific palladin (cPKOi) and control male mice.

Figure 3–Source data 2. Uncropped Western blots for Figure 3B.

Figure 3–Source data 3. Echocardiographic parameters of inducible cardiomyocyte-specific palladin knockout (cPKOi) male mice compared to controls 2 and 6 months after tamoxifen (TAM) induction.

Figure 3–Source data 4. Echocardiographic analysis on inducible cardiomyocyte-specific palladin (cPKOi) and control male mice 2 and 6 months after tamoxifen (TAM) induction.

Figure 3–Source data 5. Heart weight to body weight ratio (HW/BW) measurements on inducible cardiomyocyte-specific palladin (cPKOi) and control male mice 2 and 6 months after tamoxifen (TAM) induction.

Figure 3–Source data 6. Analysis of sarcomere shortening and Ca^{2+} transients in cardiomyocytes from inducible cardiomyocyte-specific palladin (cPKOi) and control male mice.

Figure 4–Source data 1. Cardiomyocyte (CMC) size, length, and width measurements in inducible cardiomyocyte-specific palladin (cPKOi) and control male mice 3 months after tamoxifen (TAM) induction.

Figure 4–Source data 2. Measurements of fibrotic area in the left ventricle of inducible cardiomyocyte-specific palladin (cPKOi) and control male mice 6 months after tamoxifen (TAM) induction.

Figure 4–Source data 3. Raw data for quantitative real-time PCR (qRT-PCR) on inducible cardiomyocyte-specific palladin (cPKOi) and control male mice 6 months after tamoxifen (TAM) induction.

Figure 5–Source data 1. Intercalated disc (ICD) fold amplitude measurements in inducible cardiomyocyte-specific palladin (cPKOi) and control male mice 2 and 6 months after tamoxifen (TAM) induction.

Figure 6–Source data 1. Uncropped Western blots for Figure 6A.

Figure 6–Source data 2. Densitometry on Western blots on inducible cardiomyocyte-specific palladin (cPKOi) and control male mice 2 months after tamoxifen (TAM) induction.

Figure 6–Source data 3. Quantitative real-time PCR (qRT-PCR) analysis on left ventricular biopsies from patients with dilated (DCM) and ischemic (ICM) cardiomyopathy *vs*. healthy control (Ctrl) hearts.

Figure 6–Source data 4. Uncropped Western blots for Figure 6–figure supplement 3.

Figure 6–Source data 5. Uncropped Western blots for Figure 6–figure supplement 4.

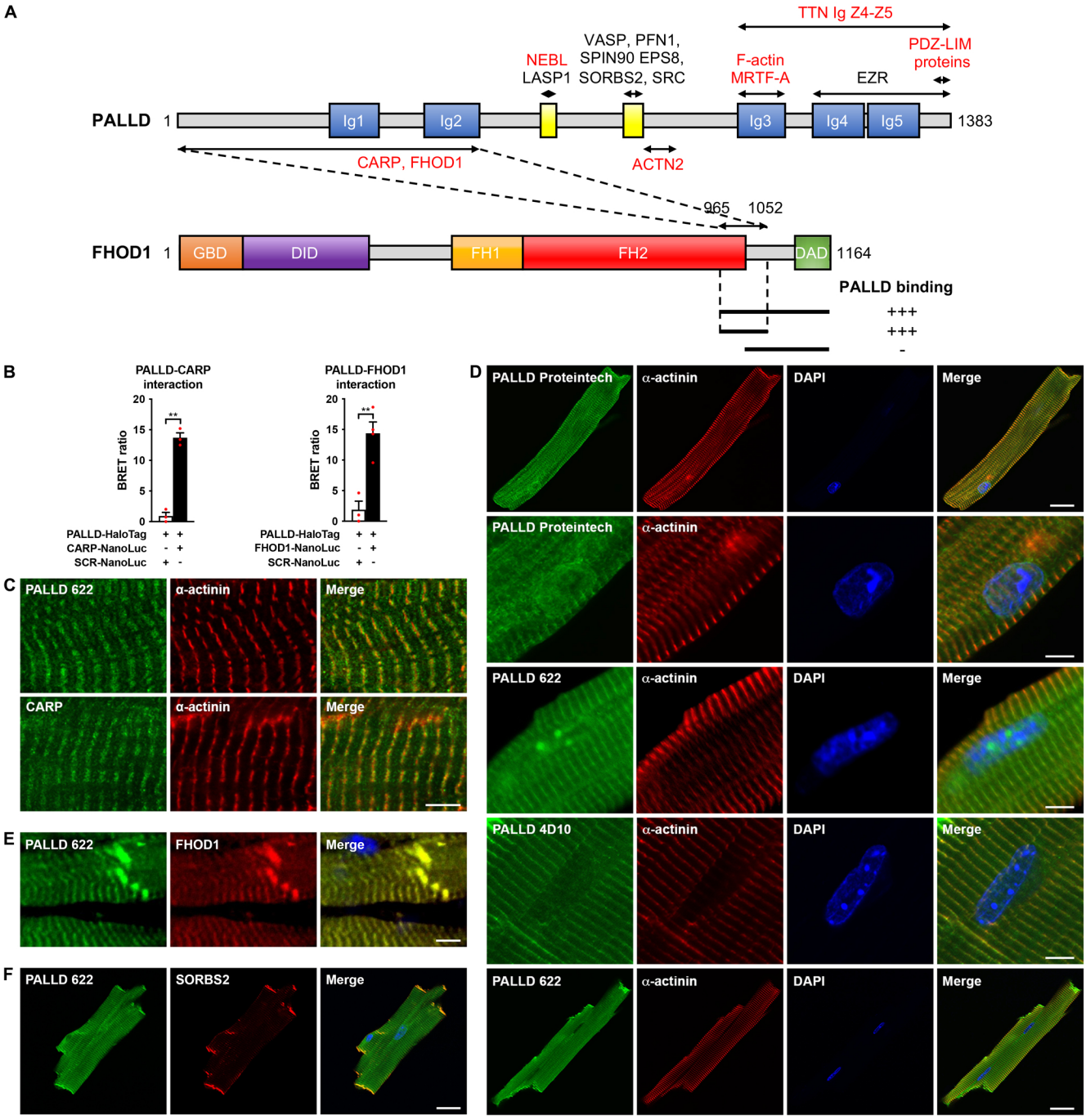

Figure 1

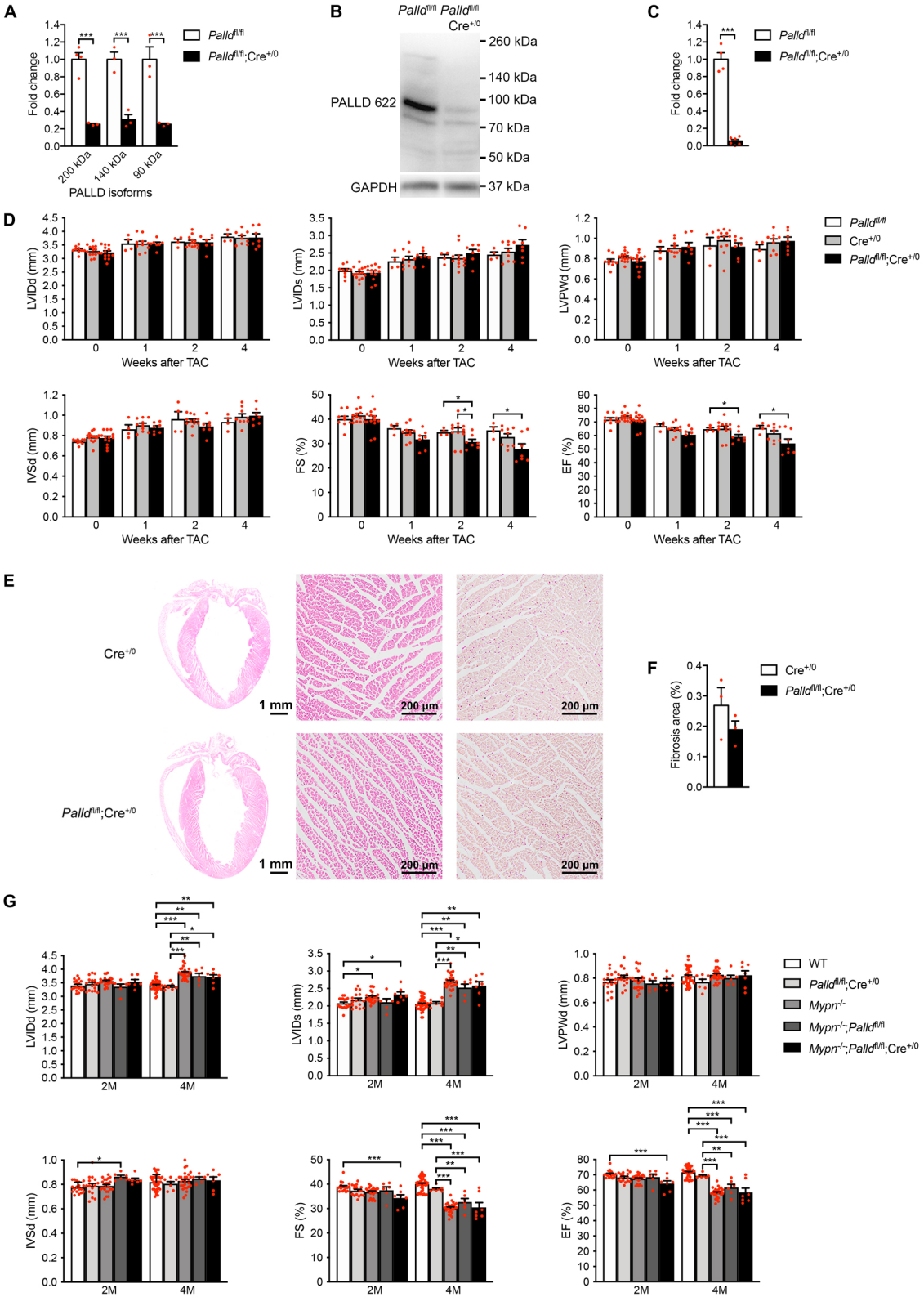

Figure 2

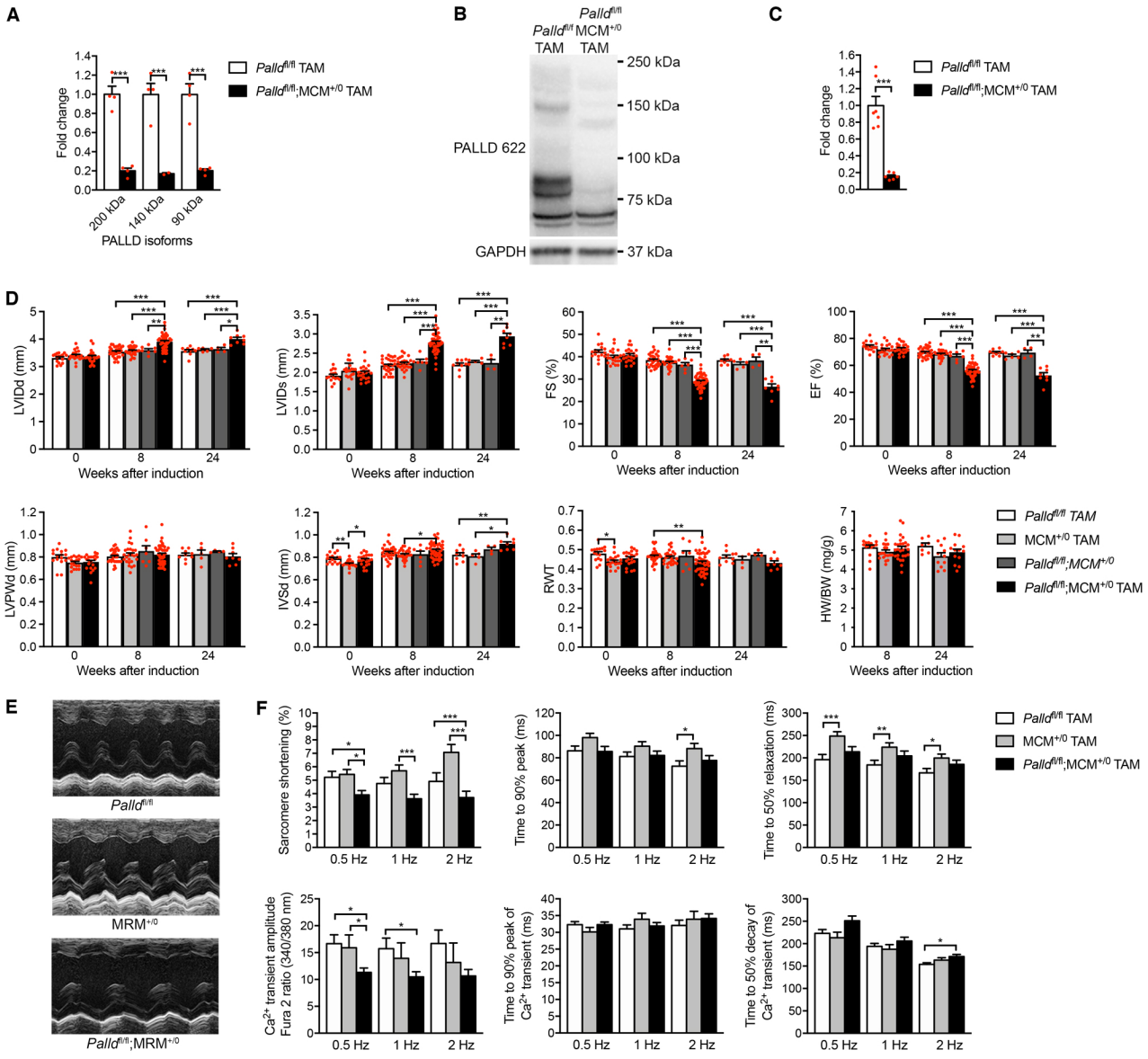

Figure 3

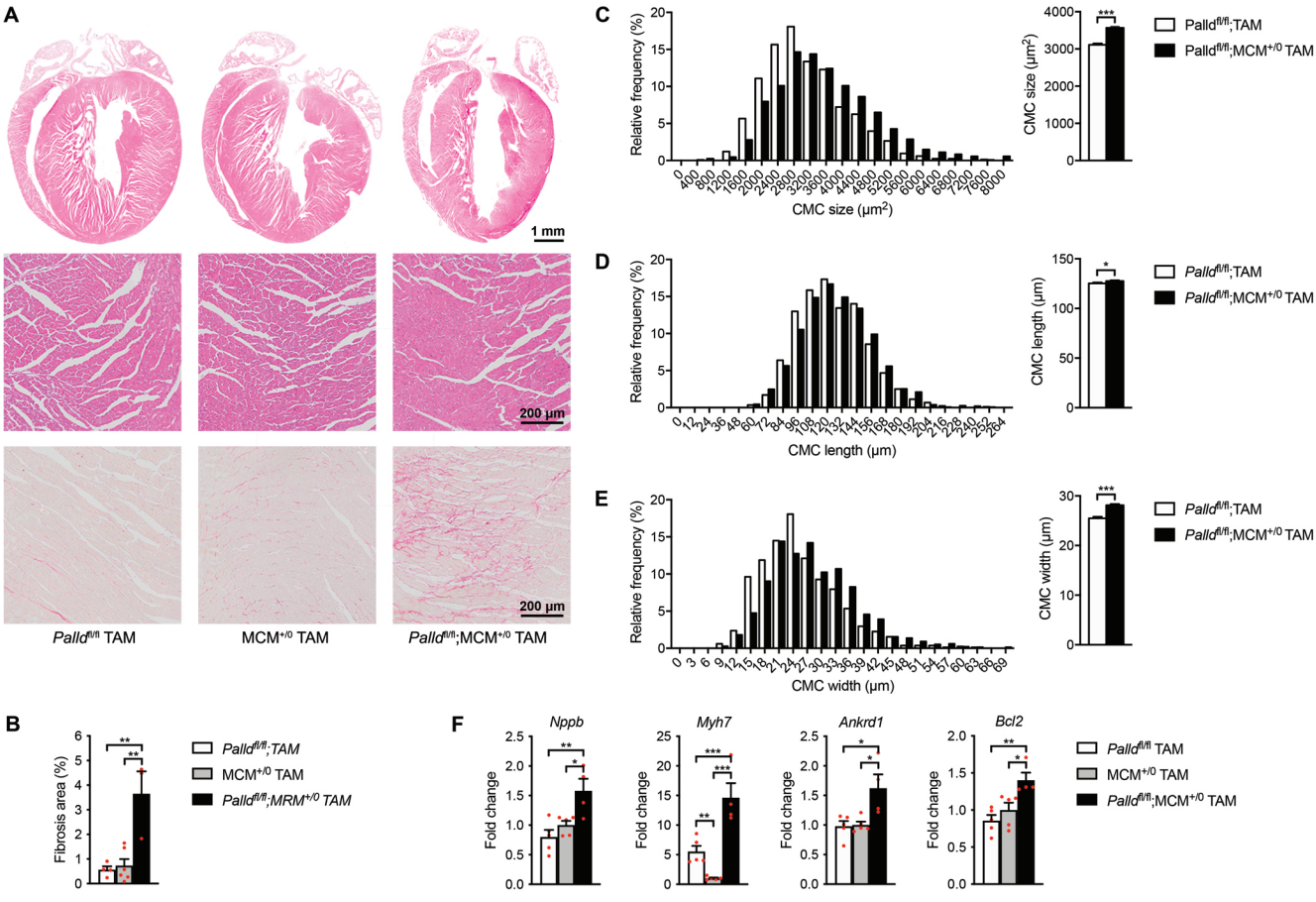

Figure 4

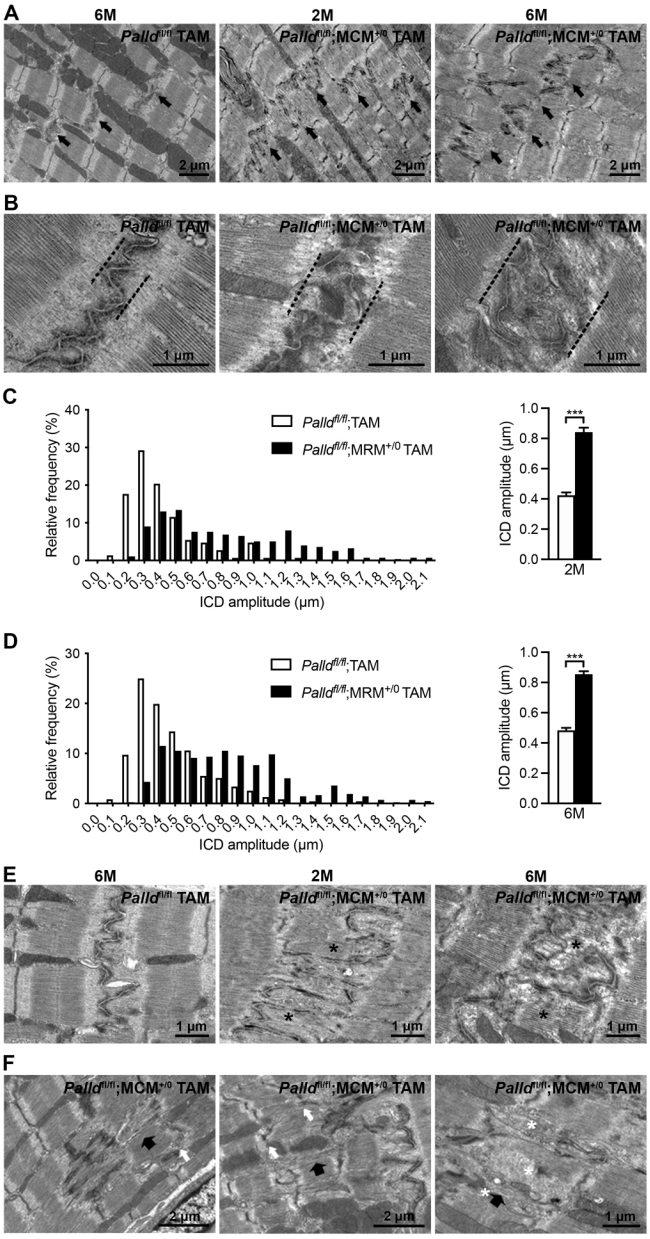

Figure 5

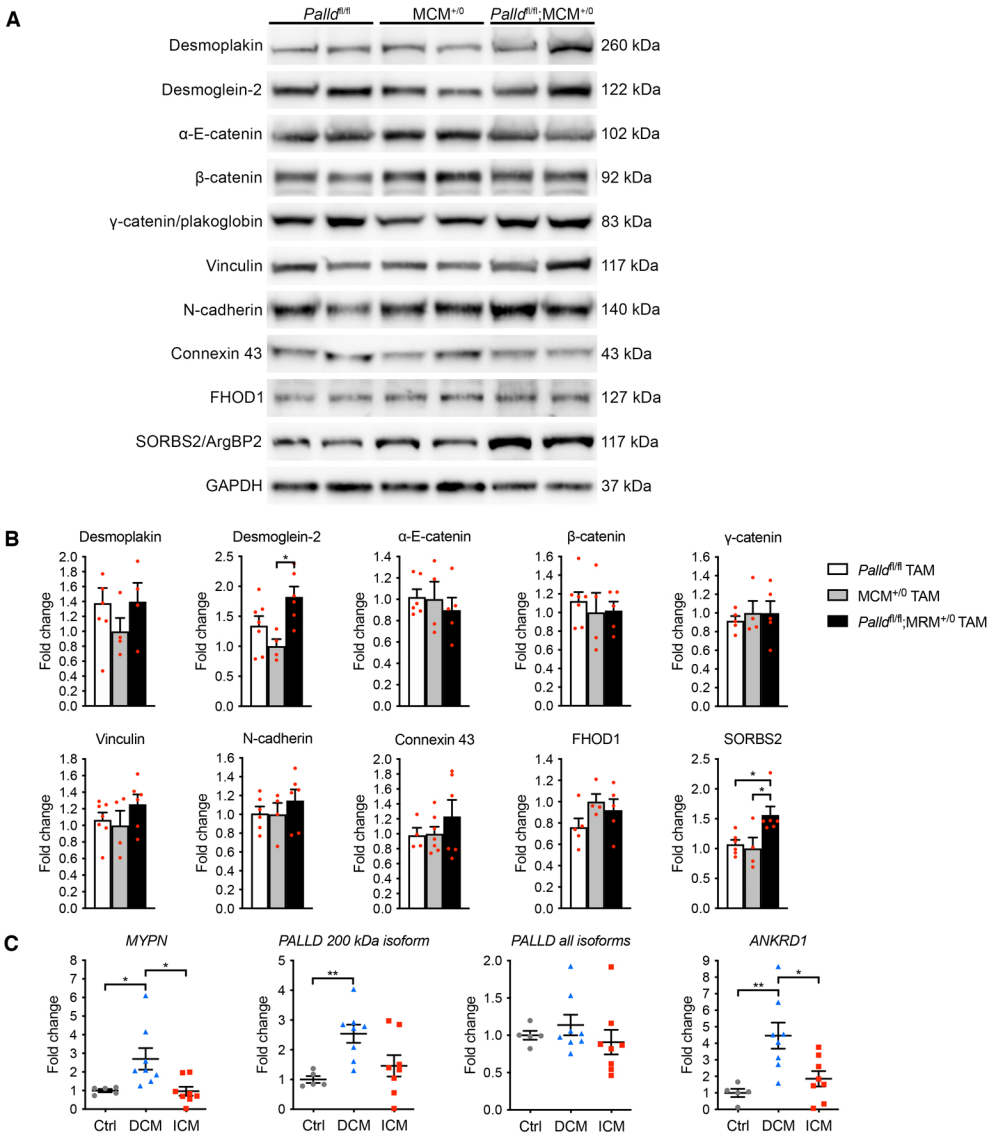

Figure 6

A

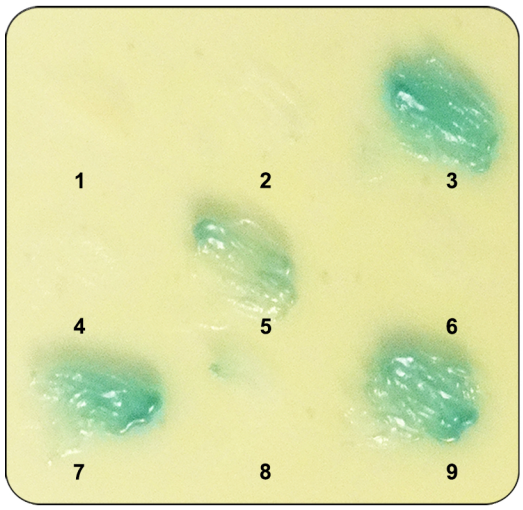

No	pGBKT7	pGADT7-AD	Interaction
1	pGBKT7	CARP	-
2	MYPN FL	pGADT7-AD	-
3	MYPN FL	CARP	+++
4	MYPN N-term (start-Ig2)	pGADT7-AD	-
5	MYPN N-term (start-Ig2)	CARP	+++
6	PALLD N-term (start-Ig2)	pGADT7-AD	-
7	PALLD N-term (start-Ig2)	CARP	+++
8	PALLD 200 kDa isoform	pGADT7-AD	-
9	PALLD 200 kDa isoform	CARP	+++

B

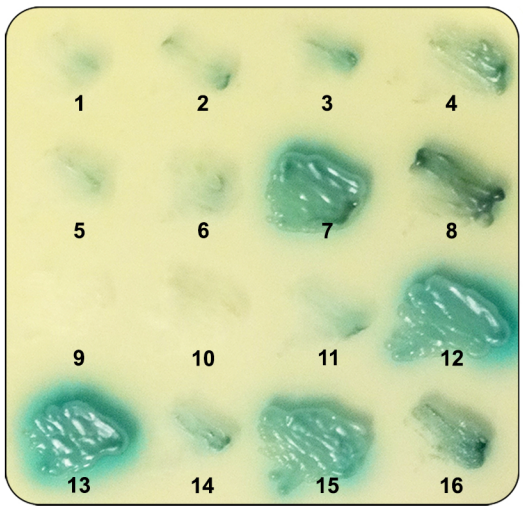

No	pGBKT7	pGADT7-AD	Interaction
1	pGBKT7	FHOD1 (3005-3607)	-
2	pGBKT7	FHOD1 (3005-3268)	-
3	pGBKT7	FHOD1 (3152-3607)	-
4	PALLD C-term (Ig3-end)	pGADT7-AD	-
5	PALLD N-term (start-Ig2)	pGADT7-AD	-
6	PALLD C-term (Ig3-end)	FHOD1 (3005-3268)	-
7	PALLD N-term (start-Ig2)	FHOD1 (3005-3268)	+++
8	PALLD N-term (start-Ig2)	FHOD1 (3152-3607)	-
9	MYPN full-length	pGADT7-AD	-
10	MYPN N-term (start-Ig2)	pGADT7-AD	-
11	MYPN C-term (Ig3-end)	pGADT7-AD	-
12	MYPN full-length	FHOD1 (3005-3607)	+++
13	MYPN full-length	FHOD1 (3005-3268)	+++
14	MYPN full-length	FHOD1 (3152-3607)	-
15	MYPN N-term (start-Ig2)	FHOD1 (3005-3268)	+++
16	MYPN C-term (Ig3-end)	FHOD1 (3005-3268)	-

Figure 1-figure supplement 1

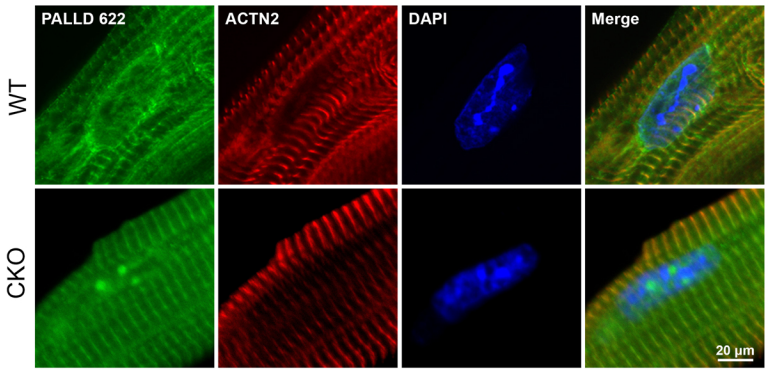

Figure 1-figure supplement 2

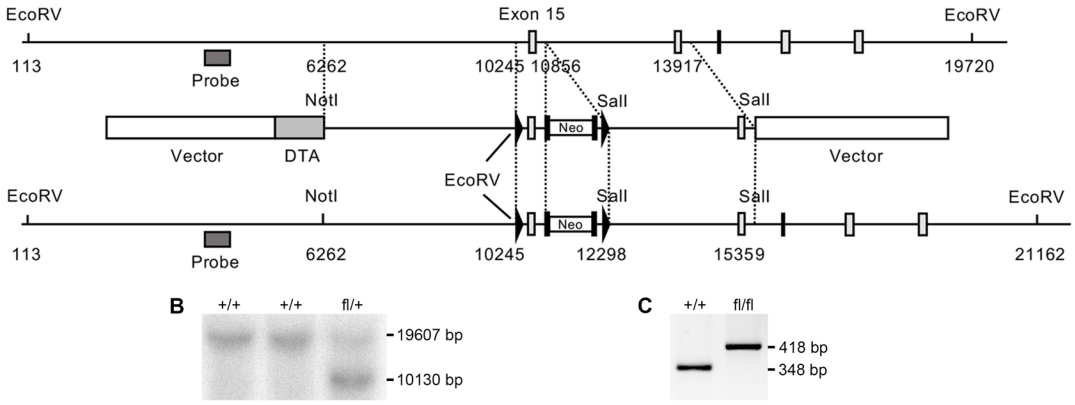

Figure 2-figure supplement 1

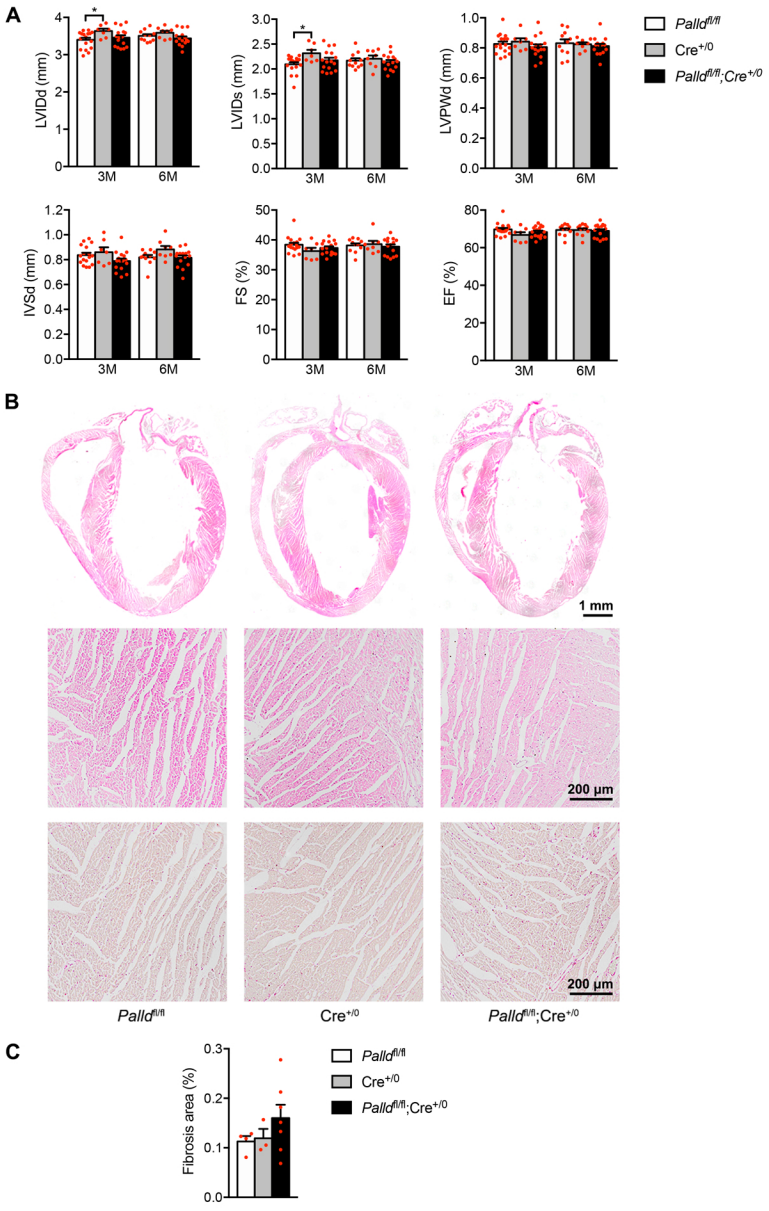

Figure 2-figure supplement 2

Figure 4–figure supplement 1. Quantitative real-time PCR (qRT-PCR) analysis on left ventricle from inducible cardiomyocyte-specific palladin knockout (cPKOi) male mice compared to controls 6 months after tamoxifen (TAM) induction.

Gene	*Palld*$^{fl/fl}$ TAM (*n* = 5)	MRM$^{+/0}$ TAM (*n* = 5)	*Palld*$^{fl/fl}$;MRM$^{+/0}$ TAM (*n* = 4)
Nppa	0.85 ± 0.28	1.00 ± 0.10	1.08 ± 0.25
Nppb	0.80 ± 0.12	1.00 ± 0.07	1.58 ± 0.21**$^{\delta}$
Myh6	0.67 ± 0.06	1.00 ± 0.05	0.72 ± 0.06
Myh7	5.52 ± 1.96	1.00 ± 0.14**	14.61 ± 2.47***$^{\delta\delta\delta}$
Actc1	0.97 ± 0.07	1.00 ± 0.05	1.01 ± 0.09
Acta1	0.50 ± 0.12	1.00 ± 0.10*	0.73 ± 0.10
Ankrd1	0.98 ± 0.09	1.00 ± 0.06	1.62 ± 0.23*$^{\delta}$
Nebl	0.87 ± 0.06	1.00 ± 0.09	0.89 ± 0.08
Ldb3	1.19± 0.33	1.00 ± 0.23	2.03 ± 0.34
Pdlim3	1.19 ± 0.08	1.00 ± 0.20	1.45 ± 0.15
Des	0.95 ± 0.03	1.00 ± 0.03	0.92 ± 0.04
Tnnc1	1.06 ± 0.02	1.00 ± 0.03	1.07 ± 0.08
Atp2a2	0.96 ± 0.05	1.00 ± 0.06	0.89 ± 0.07
Srf	1.10 ± 0.09	1.00 ± 0.05	1.16 ± 0.09
Mk11	0.86 ± 0.03	1.00 ± 0.04	0.96 ± 0.07
Col1a1	0.81 ± 0.06	1.00 ± 0.05	1.11 ± 0.16
Col3a1	0.95 ± 0.10	1.00 ± 0.08	0.96 ± 0.15
Ctgf/Ccn2	1.02 ± 0.12	1.00 ± 0.11	1.37 ± 0.18
Acta2	0.79 ± 0.11	1.00 ± 0.12	0.59 ± 0.11
Tgfb1	0.92 ± 0.06	1.00 ± 0.10	0.97 ± 0.06
Bcl2	0.86 ± 0.08	1.00 ± 0.10	1.40 ± 0.10**$^{\delta}$
Bax	0.90 ± 0.07	1.00 ± 0.06	1.12± 0.10
Tp53	0.88 ± 0.05	1.00 ± 0.09	1.06 ± 0.09
Egr1	0.76 ± 0.24	1.00 ± 0.11	1.56 ± 0.36

All values are presented as mean ± standard error of the mean (SEM). *$P < 0.05$, **$P < 0.01$ *vs*. *Palld*$^{fl/fl}$; $^{\delta}P < 0.05$, $^{\delta\delta\delta}P < 0.001$ *vs*. Cre$^{+/0}$; one-way analysis of variance (ANOVA) with Tukey's multiple comparisons test.

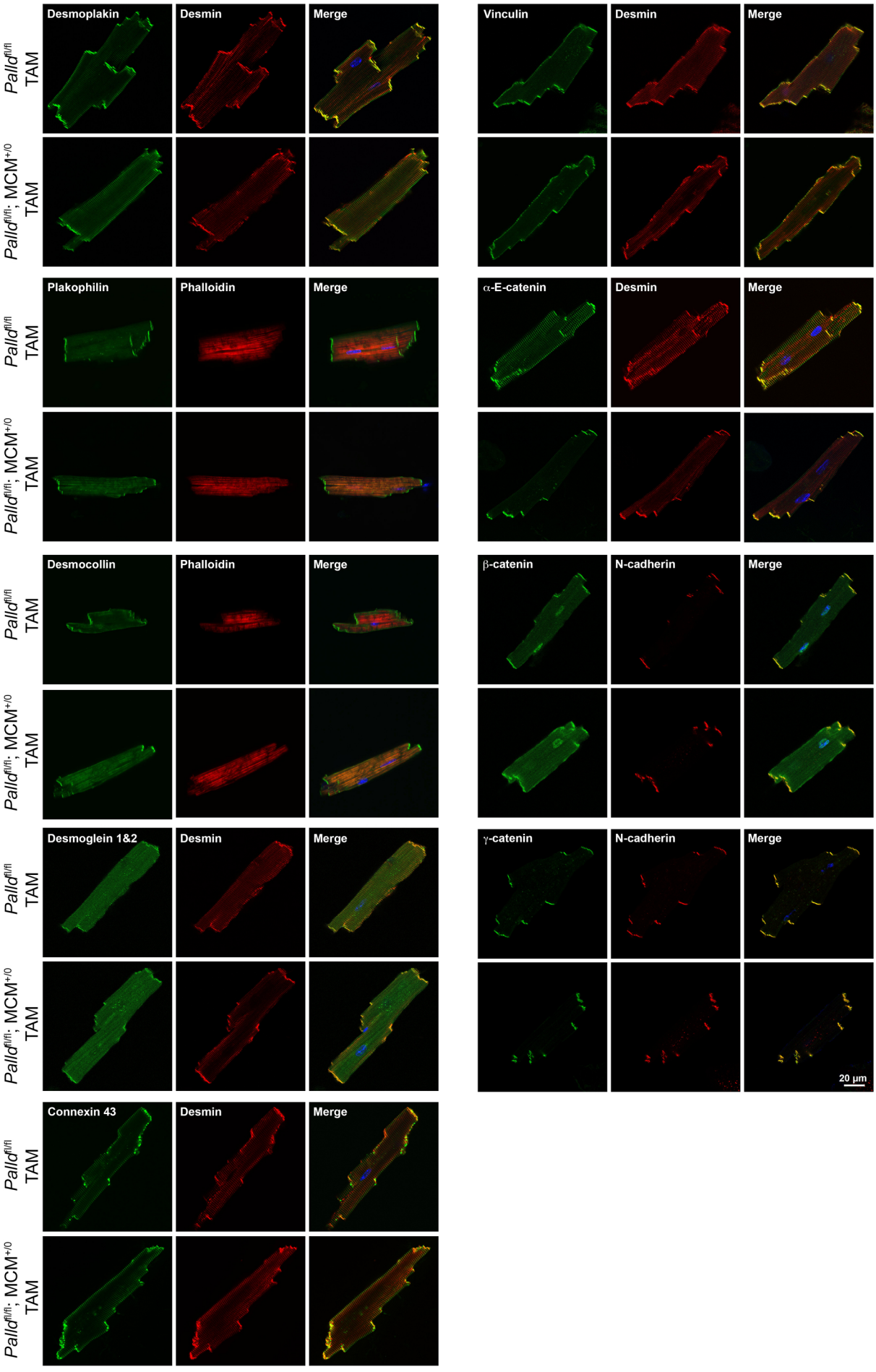

Figure 6-figure supplement 1

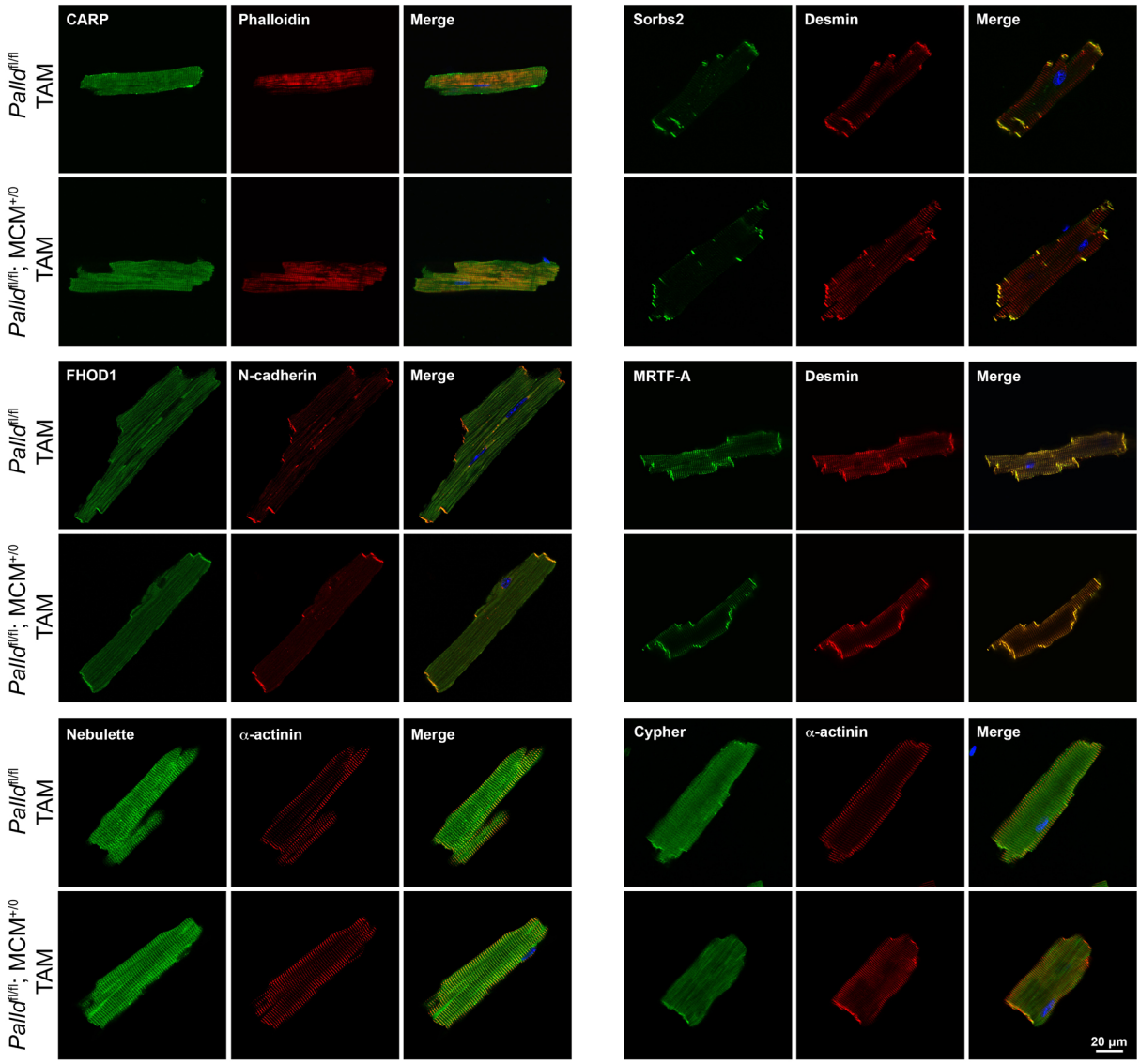

Figure 6-figure supplement 2

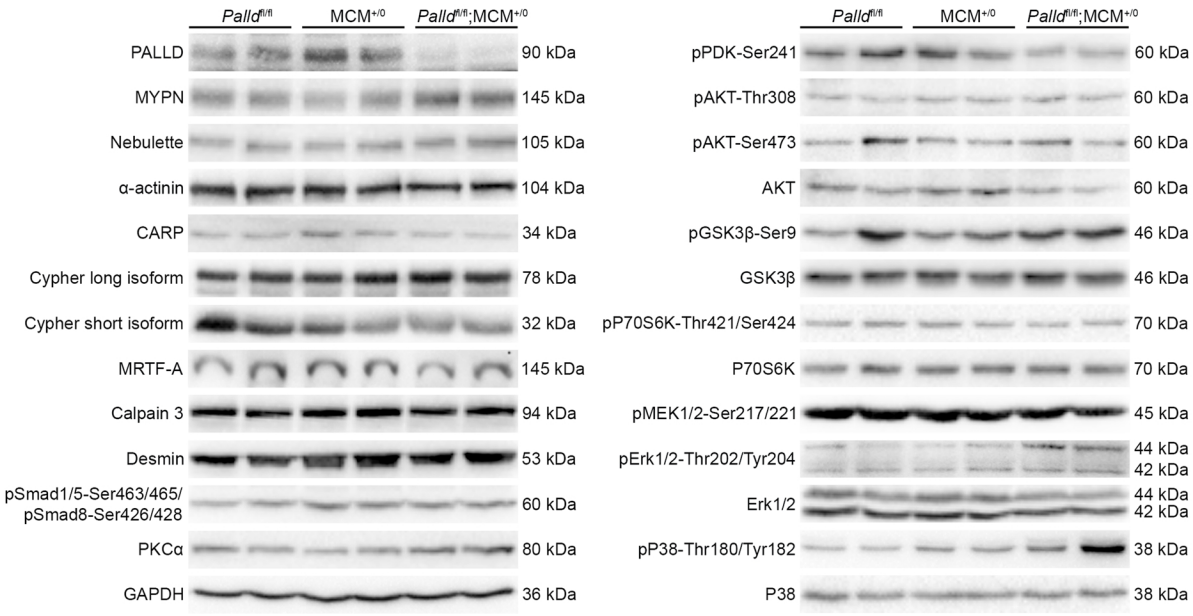

Figure 6-figure supplement 3

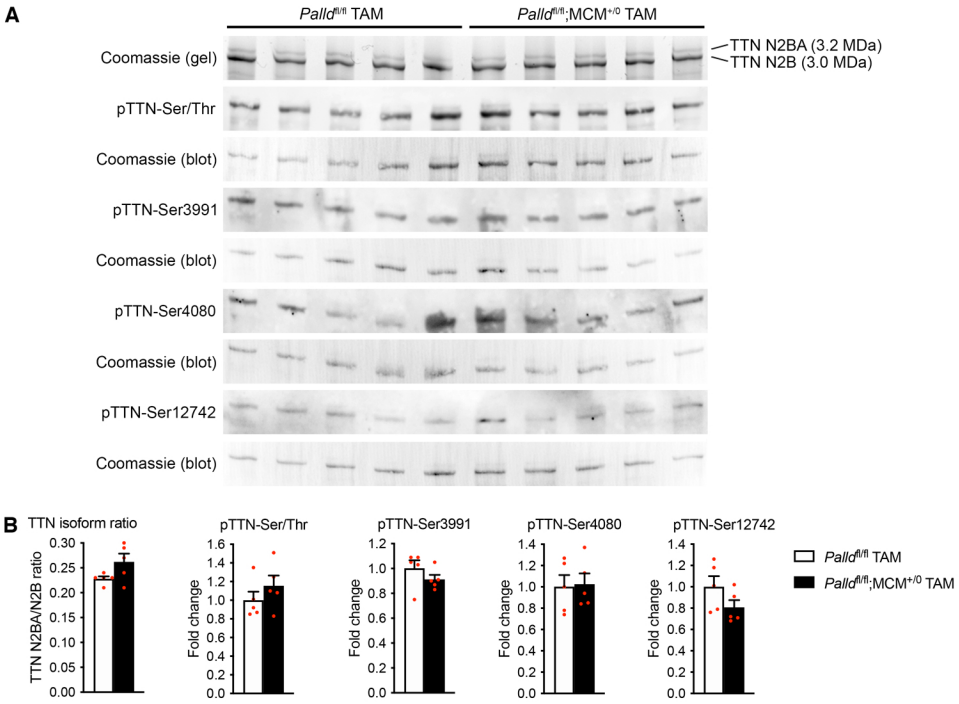

Figure 6-figure supplement 4

Figure 6–figure supplement 5. Patient characteristics.

Number	Gender	Age (years)	Disease
1	M	20-50	Ctrl
2	M	20-50	Ctrl
3	M	20-50	Ctrl
4	M	20-50	Ctrl
5	M	20-50	Ctrl
6	M	54	DCM
7	M	48	DCM
8	M	63	DCM
9	M	67	DCM
10	M	60	DCM
11	M	61	DCM
12	M	71	DCM
13	M	65	DCM
14	M	58	ICM
15	M	50	ICM
16	M	56	ICM
17	M	60	ICM
18	M	53	ICM
19	M	67	ICM
20	M	58	ICM
21	M	58	ICM

M, male; Ctrl, healthy control; DCM, dilated cardiomyopathy; ICM, ischemic cardiomyopathy.

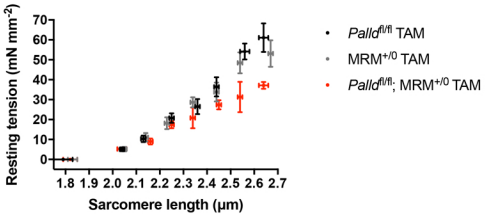

Table 1-figure supplement 1